HYDRODYNAMIC SIMULATIONS ON A GOLD NANO ELLIPSOID

A THESIS SUBMITTED TO
THE GRADUATE SCHOOL OF NATURAL AND APPLIED SCIENCES
OF
MIDDLE EAST TECHNICAL UNIVERSITY

BY

HÜSEYİN UMUT TEPE

IN PARTIAL FULFILLMENT OF THE REQUIREMENTS
FOR
THE DEGREE OF DOCTOR OF PHILOSOPHY
IN
MICRO AND NANOTECHNOLOGY

AUGUST 2024

Approval of the thesis:

HYDRODYNAMIC SIMULATIONS ON A GOLD NANO ELLIPSOID

submitted by **HÜSEYİN UMUT TEPE** in partial fulfillment of the requirements for the degree of **Doctor of Philosophy** in **Micro and Nanotechnology, Middle East Technical University** by,

Prof. Dr. Naci Emre Altun
Dean, **Graduate School of Natural and Applied Sciences** ____________

Prof. Dr. Deniz Üner
Head of the Department, **Micro and Nanotechnology** ____________

Prof. Dr. Alpan Bek
Supervisor, **Physics, METU** ____________

Assoc. Prof. Dr. Selçuk Yerci
Co-Supervisor, **Electrical and Electronic Eng., METU** ____________

Examining Committee Members:

Prof. Dr. Oğuz Gülseren
Physics, Bilkent Uni. ____________

Prof. Dr. Alpan Bek
Physics, METU ____________

Assoc. Prof. Dr. Serdar Kocaman
Electrical and Electronic Eng., METU ____________

Prof. Dr. Mehmet Emre Taşgın
Institute of Nuclear Sciences, Hacettepe Uni. ____________

Prof. Dr. Okan Esentürk
Chemistry, METU ____________

Date: 16.08.2024

I hereby declare that all information in this document has been obtained and presented in accordance with academic rules and ethical conduct. I also declare that, as required by these rules and conduct, I have fully cited and referenced all material and results that are not original to this work.

Name Last name : Hüseyin Umut Tepe

Signature :

ABSTRACT

HYDRODYNAMIC SIMULATIONS ON A GOLD NANO ELLIPSOID

Tepe, Hüseyin Umut
Doctor of Philosophy, Micro and Nanotechnology
Supervisor : Prof. Dr. Alpan Bek
Co-Supervisor: Assoc. Prof. Dr. Selçuk Yerci

August 2024, 65 pages

A hydrodynamic model is used to explore the nonlinear optical properties of a plasmonic gold nano ellipsoid. This simulation study reveals spherical harmonics in the near-field and vector spherical harmonics in the far-field. Higher-order susceptibility maps show that the nonlinear effects originate from the tips of the nano ellipsoid and that the second and third-order susceptibility values, stemming from the free electron response, are on the order of 10^{-12} $[m/V]$ and 10^{-24} $[m^2/V^2]$, respectively. Finally, four and five-wave mixing is simulated, showing equal conversion efficiencies to existing solutions. Wave mixing is useful for photon entanglement and quantum information applications.

Keywords: Plasmonics, Nonlinear, Hydrodynamic, Nanophotonics, Simulation

ÖZ

ALTIN NANO ELIPSOİT'İN HİDRODİNAMİK SİMÜLASYONLARI

Tepe, Hüseyin Umut
Doktora, Mikro ve Nanoteknoloji
Tez Yöneticisi: Prof. Dr. Alpan Bek
Ortak Tez Yöneticisi: Doç. Dr. Selçuk Yerci

Ağustos 2024, 65 sayfa

Bir altın nano elipsoit'in doğrusal dışı optik özelliklerini tespit edebilmek amacıyla serbest elektronları sıvısal hareketlerini tespit eden bir model kullanıldı. Nano elipsoit'in uç yüzeylerinde küresel harmonikler ve uzak çevresinden vektör küresel harmonikler tespit edilmiştir. İkinci ve üçüncü derece alınganlık haritaları hesaplanmıştır ve en yüksek değerler elipsoit'in uçlarında tespit edilmiştir. En yüksek ikinci ve üçüncü derece değerler yaklaşık 10^{-12} $[m/V]$ ve 10^{-24} $[m^2/V^2]$. İki farklı foton dalgaboyların doğrusal dışı etkilerden dolayı birbiriyle karışıp ve yeni dalgaboyların üretilmesi simüle edilmiştir ve elde edilen frekans çevirme oranları benzer deneysel sonuçlara yakındır. Dalga karışım etkileri kuantum dolanıklık ve kuantum enformasyon uygulamalarında kullanılmaktadır.

Anahtar Kelimeler: Plasmonik, Doğrusal dışı, Hidrodinamik, Nanofotonik, Simülasyon

ACKNOWLEDGEMENTS

I am extending thanks to my thesis advisor Prof. Alpan Bek, Prof. Emre Taşgın, Prof. Özgür Ergül, Assoc Prof. Khurram Shehzad, Dr. Zafer Artvin and Dr. Naveed Hussain.

I would also like to acknowledge the nano-optics research group members: Kamil Çınar, Murat Öztürk, Mete Günöven, Mona Zolfaghari, Ceren Korkut, Özge Demirtaş, Fırat İdikut, Burcu Karagöz, Zafer Çılgın, Nasim Esmailzad, Alp Akbıyık, Serena Erkızan and Nardin Avishan.

TABLE OF CONTENTS

LIST OF TABLES

TABLES

LIST OF FIGURES

FIGURES

LIST OF ABBREVIATIONS

ABBREVIATIONS	
SHG	Second Harmonic Generation
THG	Third Harmonic Generation
SPP	Surface Plasmon Polariton
LSP	Localized Surface Plasmon
3WM	Three-Wave Mixing
4WM	Four-Wave Mixing
5WM	Five-Wave Mixing
SFG	Sum Frequency Generation
DFG	Difference Frequency Generation
PML	Perfectly Matched Layers
DA	Dipole Antenna
DRA	Doubly Resonant Antenna

CHAPTER 1

INTRODUCTION

Nonlinear optics is a phenomenon where the excited oscillation moves differently to the incident wave during intense excitation. Higher or lower frequency modes arise in the nonlinear material, where the new frequencies are either integer multiplication, sum, or difference of the incident fundamental frequencies. The first nonlinear experiment (second harmonic generation) was realized with the advent of lasers, outputting high-intensity coherent light [1]. Examples of nonlinear optical phenomena are second and third harmonic generation (SHG & THG), where two and three photons are combined to produce new photons with double and triple the energy, respectively. Wave mixing is another nonlinear optical effect where multiple input frequencies and their higher harmonic generation mix to create new frequencies.

Examples of interesting THG applications are direct image processing in a Fourier plane, which is used to resolve a heavily distorted image that has passed through a dispersive media [2], and thermal imaging with silicon image sensors [3].
Birefringent crystals are commonly used in SHG and THG, adhering to phase-matching conditions and where their sizes determine the conversion efficiency [4]. However, phase-matching is not required for subwavelength nanoparticles [4] as near-fields act as the primary mechanism [5], allowing significant miniaturization. Semiconducting nanoparticles have become popular in second and third-harmonic generation studies [6, 7, 8], which are damage-resistant to intense irradiation and have high third-order susceptibilities [5]. Silicon and germanium are examples of centrosymmetric lattices, suitable for third harmonic generation at shorter wavelengths (near-IR to UV);

While semiconductors are transparent beyond near-infrared wavelengths, gold is excellent at absorbing photons of longer wavelengths. Single-mode, long-range optical communication uses the 1.55 μm band. Gold is ideal at absorbing short-wavelength infrared (>1.4 μm) photons and beyond. Bulk gold naturally supports third harmonic generation due to its centrosymmetric lattice, but not second harmonic generation. The second-order effects can be realized through the nonlinear free electron response in asymmetrical or large metal nanoparticles (multipole excitation) [9, 10]. Plasmonic nanoparticles also stand out due to high optical absorption (relative to their sizes), and altering the size and shape adjusts the absorption peak (frequency selectivity) [11]. A corresponding change in bulk media requires a different material. High-resolution fabrication processes of metals are widely available today [12], enabling studies of exotic metal meta-materials such as split-ring resonators [13] or light-confining bowtie antennae [14].

Simulation is integral to any experimental study. Low-intensity plasmonics are simulated by using Maxwell's equations with linear dielectric terms. Excitation by a high-power femtosecond pulse requires modeling nonlinear material properties, where a popular method is adding nonlinear terms to the dielectric function [15]. These terms are often assumed homogeneous, which is valid for the third-order susceptibility. However, bulk gold does not support even order nonlinearities; therefore, the even order susceptibility cannot be modeled accurately with added homogeneous terms.

Furthermore, the assumed susceptibility values originate from experimental results, which may vary greatly depending on methodology [16]. This study uses a hydrodynamic model to circumvent estimated dielectric functions. Ginzburg et al. have previously used a similar nonperturbative hydrodynamic model (regarding free electrons as a charged fluid, accelerated by the Lorenz force) to simulate nonlinearity in infinitely long 2D gold nanorods [17].

Here, the hydrodynamic model is extended to three-dimensional gold nano ellipsoids. Different aspect ratios and cylindrical rods with different tips are simulated. Several nonlinear optical properties are studied. The scattered far-fields are plotted and compared with Mie theory. The near-fields on the surface of the gold nano ellipsoid are compared with spherical harmonics, the effects on the spectra during modulation of incident power are studied, higher order susceptibility maps are plotted, and four/five wave mixing is simulated. Photon entanglement is possible in four and five-wave mixing (4WM & 5WM) and has potential uses in future quantum information applications.

1.1 Bulk Plasmons

Derivation of the bulk plasmon equation is started with Maxwell's equations [18]:

$$\frac{\partial \vec{J}}{\partial t} + \epsilon_0 \frac{\partial^2 \vec{E}}{\partial t^2} = -\frac{1}{\mu_0} \nabla \times (\nabla \times \vec{E}) \tag{1.1.1}$$

, which stems from Ampere's cicuital law; a time-derivative is added on both sides, and the curl of the magnetic field is expressed by a double curl of the electric field (Maxwell-Faraday equation). Next, the time-derivative of the current density is expressed as:

$$\frac{\partial \vec{J}}{\partial t} = \frac{Ne^2}{m} \vec{E} \tag{1.1.2}$$

, where N is the electron density, e is the electron charge, and m is the electron mass. The factor before the electric field vector is also the plasma frequency squared.

$$\omega_p^2 \vec{E} + \epsilon_0 \frac{\partial^2 \vec{E}}{\partial t^2} = -\frac{1}{\mu_0} \nabla \times (\nabla \times \vec{E}) \tag{1.1.3}$$

Two electric field components are introduced in Equation 1.1.3, a transverse and a longitudinal component.

$$\frac{\partial^2 \vec{E}}{\partial t^2} + \omega_p^2 \vec{E}_t - c^2 \nabla^2 \vec{E}_t = -\left(\frac{\partial^2 \vec{E}_l}{\partial t^2} + \omega_p^2 \vec{E}_l\right) \tag{1.1.4}$$

Separating the right-hand-side expression leads to the longitudinal bulk plasmon equation.

$$\frac{\partial^2 \vec{E}_l}{\partial t^2} + \omega_p^2 \vec{E}_l = 0 \tag{1.1.5}$$

Here, the longitudinal bulk plasmons oscillate only at the plasma frequency. Bulk plasmons cannot be excited by transverse photons; longitudinal excitation is required, such as directing an electron beam into the metal. If the metal is thin, the exiting electron beam will have energy less or greater in steps of $\hbar\omega_p$. Separating the transverse left-hand side in Equation 1.1.4 gives the equation for the transverse component. However, the dispersion relation for the transverse bulk component does not intersect with the dispersion relation of photons, which hinders photon-to-bulk plasmon coupling. Photons would necessitate velocities greater than the speed of light, which is impossible.

1.2 Surface Plasmons

Surface plasmons are different from bulk plasmons due to the metal-dielectric boundary interface. In short, oscillating fields, propagating in the direction of the interface, and evanescent exponentially decaying fields in the normal direction of the surface are present. The dispersion relation is derived by assuming surface waves and implementing the electromagnetic interface condition [18]:

$$k = \frac{\omega}{c}\sqrt{\frac{\epsilon_m \epsilon_d}{\epsilon_m + \epsilon_d}} \tag{1.2.1}$$

, where k is the wave-vector, ω is the angular frequency, $\epsilon_m$is the dielectric function of the metal and ϵ_d is the dielectric function of the dielectric. Figure 1.2.1 is obtained by plotting the surface plasmon dispersion relation (Equation 1.2.1), where the dielectric function of the free metals is assumed as the following:

$$\epsilon_m = 1 - \frac{\omega_p^2}{\omega^2} \tag{1.2.2}$$

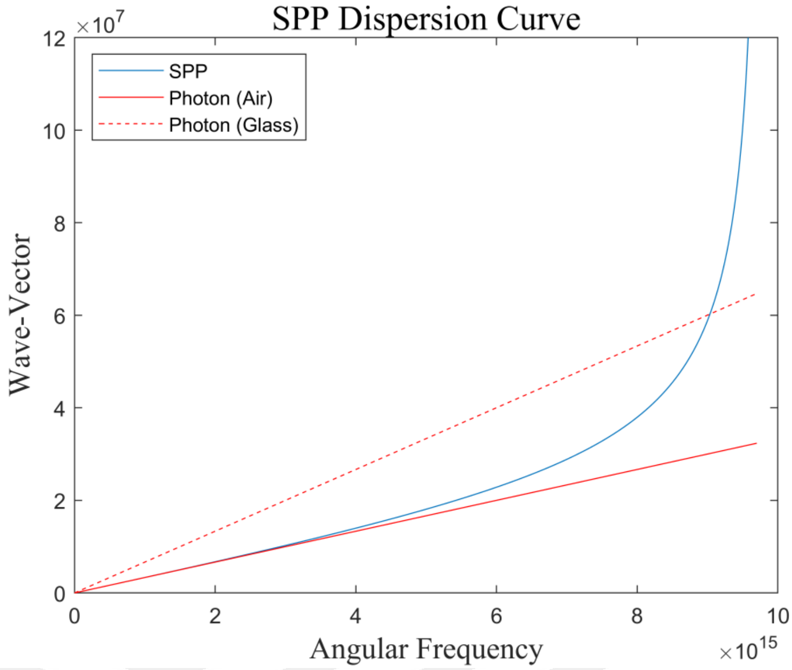

Figure 1.2.1: The surface plasmon dispersion relation is given by Equation 1.2.1, which is plotted and compared with the dispersion relation of photons.

In Figure 1.2.1, surface plasmons do not couple directly with photons in air or vacuum and require a dielectric above the metal surface.

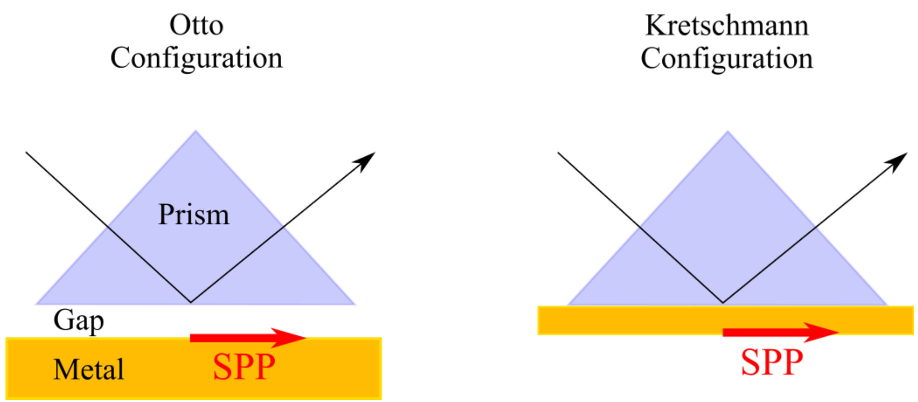

Figure 1.2.2: Two different configurations of SPP to photon coupling.

Figure 1.2.2 illustrates two common techniques to couple photons to surface plasmons: the Otto and Kretschmann configurations. Other methods of coupling photons to SPPs are gratings and near-fields [19]. Generally, SPPs suffer from attenuation, limiting their use to micrometer lengths scales [20]. However, large local field intensities can be achieved, which is useful in many applications such as molecule detection.

1.3 Localized Surface Plasmons

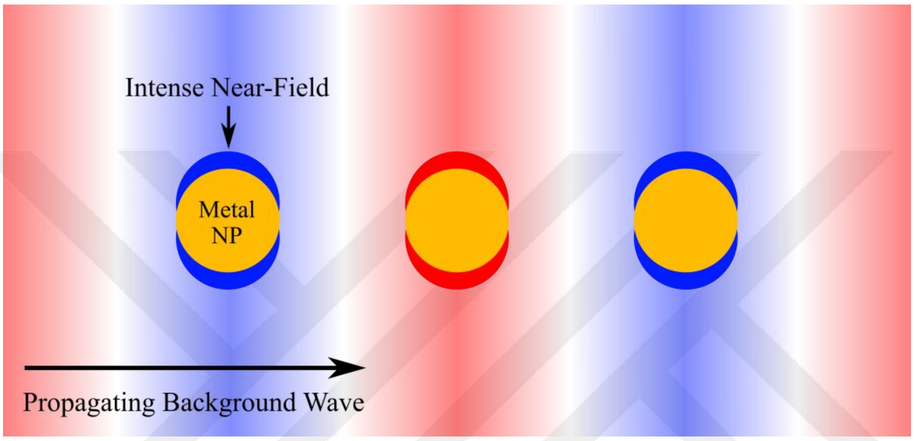

Figure 1.3.1: Free electrons oscillate in harmony with the background wave, creating intense near-fields.

Plasmon oscillations in metal nanoparticles differ from bulk and surface plasmons as special conditions in dielectric surroundings or photon incident angles are not required for photon coupling. The excited plasmon modes are confined to the nanoparticle's surface, which are smaller than the wavelength of light, and are therefore called localized surface plasmons (LSP). LSPs are often described as oscillating electron cloud perturbations. However, expressing the phenomenon in terms of electric fields is more intuitive. Figure A.1 in the appendices section shows the hydrodynamical results of electron accumulation at a nano ellipsoid surface. Only under extreme illumination conditions do many electrons accumulate at the opposite ends of the nano particle. Under more realistic illumination conditions, the accumulated electron number density is far below the density of a single electron, meaning that the free electron cloud is perturbed very slightly.

Therefore, the illustration of localized plasmons as oscillating electrons subject to a restoring force similar to a spring action is inaccurate.

Figure 1.3.1 illustrates the first-order excited near-fields that are vertically polarized, and the electron cloud will likewise move vertically in harmony with the background frequency. The situation changes with higher-order excitations, which are not solely vertically oriented. The higher-order fields are presented in the results section.

Near-fields have peculiar properties; the magnetic and electric fields are out of phase, and their phase velocities differ from the speed of light [21]. Unlike transverse plane waves in the far field, near-fields have an electric radial component on metal surfaces, which decays rapidly with increasing distance from the radiating surface [22].

The near-fields in Figure 1.3.1 are greatly simplified, only illustrating the first-order mode in one polarization direction. At higher excitation intensities, higher orders of fields are created. These modes create a local polarizability, which differs from the bulk material polarizability. This artificially created polarizability is the reason why metal nanoparticles have different optical properties to their bulk form; bulk gold has a yellow color, while gold nanospheres can have a red color. The optical properties depend on the surrounding dielectric, material, size, shape, periodicity, and illumination intensity.

1.4 Mie Scattering

Light scattering properties of larger particles are far from uniform. Mie scattering predicts the scattering of larger dielectric spherical objects. Helmholtz’s equations for the magnetic and electric fields are:

$$\nabla^2\vec{E} + k^2\vec{E} = 0 \tag{1.4.1}$$

$$\nabla^2\vec{H} + k^2\vec{H} = 0 \tag{1.4.2}$$

The Laplace operators indicate source-free conditions. The following **L**, **M,** and **N** are solutions to the Helmholtz equations above, satisfying the divergence-free condition:

$$\vec{L} = \nabla\psi \tag{1.4.3}$$

$$\vec{M} = \nabla \times (\vec{r}\psi) \tag{1.4.4}$$

$$\vec{N} = \frac{1}{|\vec{k}|}\nabla \times \vec{M} \tag{1.4.5}$$

Here, ψ is a scalar function. The longitudinal modes are represented by **L**, the magnetic modes by **M**, and the electric modes by **N**. The magnetic and electric modes are vector spherical harmonics. The series of modes of vector spherical harmonics depends on the boundary conditions and the sphere's radius, leading to a size-dependent extinction cross-section. The series of modes begins with first-order dipoles and second-order quadrupoles and continues with ever higher modes. The extinction cross-section is proportional to $\left(|\vec{k}|R\right)^{2L+1}$, where $\vec{k}$ is the wave vector, R is the radius, and L is the mode order. For small particles, the electric mode consists purely of a dipole. Higher-order modes are only available with larger particle sizes.

1.5 Motivation

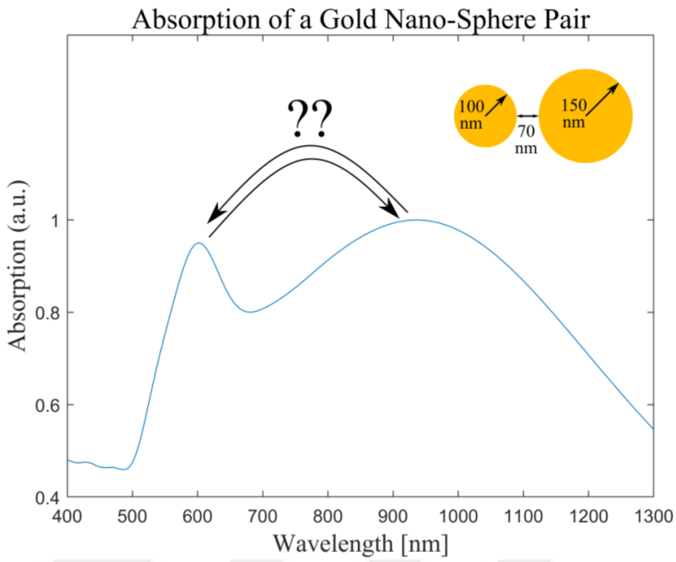

Figure 1.5.1: A typical absorption spectrum of a composite plasmonic system consisting of two differently sized particles spaced relatively close. A similar effect can also be achieved with two identical particles with a small gap.

Figure 1.5.1 illustrates a typical absorption spectrum of a pair of gold nanospheres. The two differently sized nanoparticles and the gap size determine the two absorption peaks. Similar properties can also be achieved with two identical nanospheres, where the near-field in the nanometer-sized gap couples the two nanospheres, effectively creating a larger combined particle. The exemplified pair in Figure 1.5.1 can resonate at two different wavelengths and be enhanced by fabricating the pair in an array. However, due to the lınear response, converting one wavelength into another is usually impossible with plasmonic nanoparticles. In order to create a nonlinear response, much stronger electric fields are required, and near-field confinement through sharp tips and narrow gaps does not provide the necessary field strengths. Mathematically speaking, a phenomenological term,

$$\vec{P} = \epsilon_0(\chi^{(1)}\vec{E} + \chi^{(2)}\vec{E}^2 + \chi^{(3)}\vec{E}^3 + h.o.t.) \tag{1.5.1}$$

, could be added to a simulation model, but it would be unphysical. The motivation was to explore a physical path for frequency conversion and mixing. The idea was to explore if a turbulent free electron flow at the sharp tips of a nanoparticle could lead to nonlinearity.

1.6 Hydrodynamic

Maxwell's and Navier-Stokes' equations are combined to model free electrons [17]. The source frequency is below the plasma frequency of gold, and restoring forces are not considered. The set of equations constituting the hydrodynamical model is the following:

$$\nabla \times (\nabla \times \vec{E}) + \frac{\partial_{tt}\vec{E}}{c^2} + \mu_0 \partial_{tt}\vec{P} = 0 \tag{1.6.1}$$

$$m_e n(\partial_t \vec{v} + (\vec{v} \cdot \nabla)\vec{v} + \gamma\vec{v}) = -en(\vec{E} + \vec{v} \times \vec{H}) - \vec{\nabla} p \tag{1.6.2}$$

$$p = \frac{\hbar^2 (3\pi^2)^{\frac{3}{2}}}{5m_e} n^{5/3} \tag{1.6.3}$$

$$\partial_t n + \nabla \cdot (n\vec{v}) = 0 \tag{1.6.4}$$

$$\partial_t \vec{P} = -en\vec{v} \tag{1.6.5}$$

, where c is the speed of light, m_e is the electron mass, n is the electron density, γ is the damping parameter ($\gamma_{Au} = 1.075 \cdot 10^{14}\ s^{-1}$), and p is the photon pressure of a Fermi gas. Equation 1.6.1 is our regular wave equation. Navier-Stokes' equation (Equation 1.6.2) is used instead of an effective dielectric function ε(ω). The polarization density relation (Equation 1.6.5) couples electron densities and velocities with the wave equation (Equation 1.6.1). The continuity equation (Equation 1.6.4) enforces the confinement of free electrons. The hydrodynamic model assumes that the cloud of electrons form a continuum, which is true for larger particle sizes. The mean electron scattering length in gold is 37.7-42 nm [11, 23]. The short axes of the ellipsoids and rods were limited to 40 nm in diameter to ensure that the hydrodynamic model works in a continuum environment. The hydrodynamic model is not expected to be accurate for small nanoparticles.

1.7 Boundary Conditions

In addition to the set of hydrodynamic equations, the standard electromagnetic interface conditions between the metal and vacuum are implemented.

$$\vec{n} \times (\vec{E}_2 - \vec{E}_1) = \vec{0} \quad (1.7.1)$$

$$(\vec{D}_2 - \vec{D}_1) \cdot \vec{n} = \sigma_s \quad (1.7.2)$$

$$(\vec{B}_2 - \vec{B}_1) \cdot \vec{n} = 0 \quad (1.7.3)$$

$$\vec{n} \times (\vec{H}_2 - \vec{H}_1) = \vec{J}_s \quad (1.7.4)$$

The indices 1 and 2 indicate the different medium, **n** is the normal vector on the metal-vacuum interface, σ_s is the surface charge density, and $\vec{J}_s$ is the surface current density.

1.8 Source

The source is a Gaussian pulse, with its polarization along the long axis of the gold nano-ellipsoid:

$$\vec{E}_{in} = \hat{y} E_0 e^{i\omega t} e^{-a(t-t')^2} \quad (1.8.1)$$

, here $\omega = 1.21 \cdot 10^{15}\ rad/s$ (λ=1560 nm), time-offset is $t' = 1.5 \cdot 10^{-13}\ s$, $a = 6.1 \cdot 10^{26}\ s^{-2}$. The pulse length is $\tau_{Pulse} = 67.2\ fs$ at 1560 nm, below the limit of dephasing time scales [24] and above 15 fs, allowing the electrons to form modes [25]. The pulse amplitude of $E_0 = 10^{12}\ V/m$ is below the melting threshold of gold [17].

Different aspect ration ellipsoids are simulated with 1234 and 1790 nm. Their pulselengths are adjusted to maintain the equivalent number of oscillations within the Gaussian pulse. The pulselengths for the 1234 and 1790 nm sources are 53.5 and 77.6 fs, repectively. For wave-mixing simulations, a secondary 1300 nm wavelength pulse is added to the four wave mixing simulations. A 570 nm pulse is added to the three wave mixing simulations.

1.9 Simulation Domain

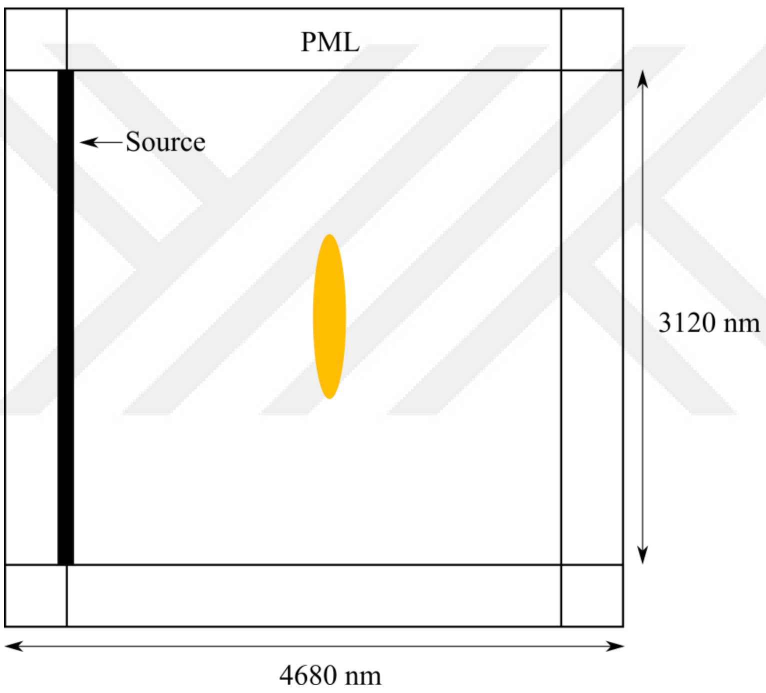

Figure 1.9.1: Simulation domain of the hydrodynamical simulations.

Figure 1.9.1 illustrates the cross-section of the cylindrical simulation domain. One wavelength’s length (1560 nm) was used to space the centered gold nano ellipsoid to the inner PML surfaces. PML thickness was set to half a wavelength, equally on each side. Coarser and finer mesh were used on the outer and ellipsoid parts of the domain, respectively. Rectangular prism mesh was used in the PML domain, and tetrahedral mesh elsewhere. Maximum and minimum mesh size was 60 and 2 nm, respectively. Additional boundary conditions were used on the outer PML boundaries, where the electric fields and their spatial derivatives were set to zero.

The total simulation time is $1.6 \cdot 10^{-12}\ s$, and the time between solution steps is $4 \cdot 10^{-16}\ s$, sampling the shortest wavelength (THG, 520 nm) at least four times per wave cycle. COMSOL Multiphysics simulation program was used to simulate the hydrodynamical model.

CHAPTER 2

NEAR- AND FAR-FIELDS

2.1 Ellipsoids

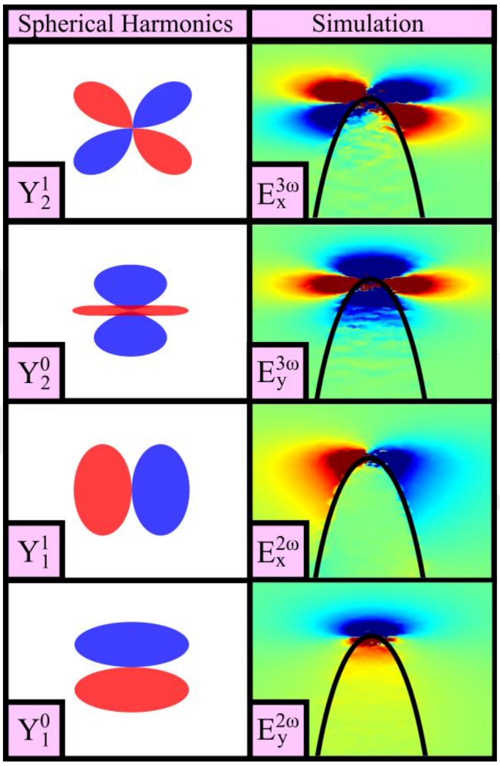

Figure. 2.1.1: Spherical Harmonics, comparison between simulated electric fields (at each harmonic and polarization) with spherical harmonic counterparts. Each harmonic constitutes a unique state.

Figure 2.1.1 compares simulated electric fields at the tip of the nano-ellipsoid and spherical harmonics. Each harmonic and polarization constitutes a spherical harmonic. Each spherical harmonic is orthogonal to one another, implicating that unique energy states exist on the tips of the gold nano ellipsoid during intense photon illumination. The electric fields in Figure 2.1.1 are obtained by performing

Fourier transforms on each time-dependent electric field polarization component in a spatial grid, isolating the relevant frequency, and plotting the time-averaged fields. Analytic solutions do not exist for nonlinear equations. However, Frazer has previously shown that an infinite series of spherical harmonics are solutions (zero divergence toroidal and poloidal fields) to the incompressible Navier-Stokes equation [26]. This study uses a compressible form (non-zero divergence) of the Navier-Stokes' equation to model a Fermi gas, and the solutions likewise consist of spherical harmonics. Interestingly, spherical harmonics are also the solutions to electron orbitals in hydrogen-like atoms. It might be possible to manipulate or extract orbital information of a single atom placed in the vicinity of the gold nanoellipsoid.

Near-field dynamics are governed by the Navier-Stokes equation. However, the Navier-Stokes' equation is only valid inside the nano particle and does not govern the external scattered far-field modes. Therefore, near-fields in Figure 2.1.1 are not to be confused with vector spherical harmonics, which are the solutions to the source-free Helmholz equation (Mie scattering) [10]. The simulated far-field modes are plotted in Figure 2.1.3 and consist of vector spherical harmonics. The hydrodynamic model aligns with Mie theory in the far-field, which is expected since the air domain is modeled after the source-free Maxwell's equations.

Sukharev et al. have simulated similar gold nanorods using an FDTD method, and the obtained electric fields are similar [27]. Sukharev does not present third-order electric fields but provides first and second-order results. In general, FDTD results in smeared fields. Comparatively, the electric fields in this thesis are located on the particle surfaces.

In addition to the original nanoellipsoid (optimized for 1560 nm), larger and smaller aspect ratio simulations are added. The diameter is maintained, but the length is changed from 256 nm to 300 and 200 nm for the shorter and longer nanoellipsoids, respectively. The larger and the smaller aspect ratio ellipsoids have their absorption peaks at 1790 and 1234 nm, respectively. The excitation source was adjusted accordingly. Figures 2.1.4 and 2.1.5 show that the spherical harmonics are nearly identical to Figure 2.1.2.

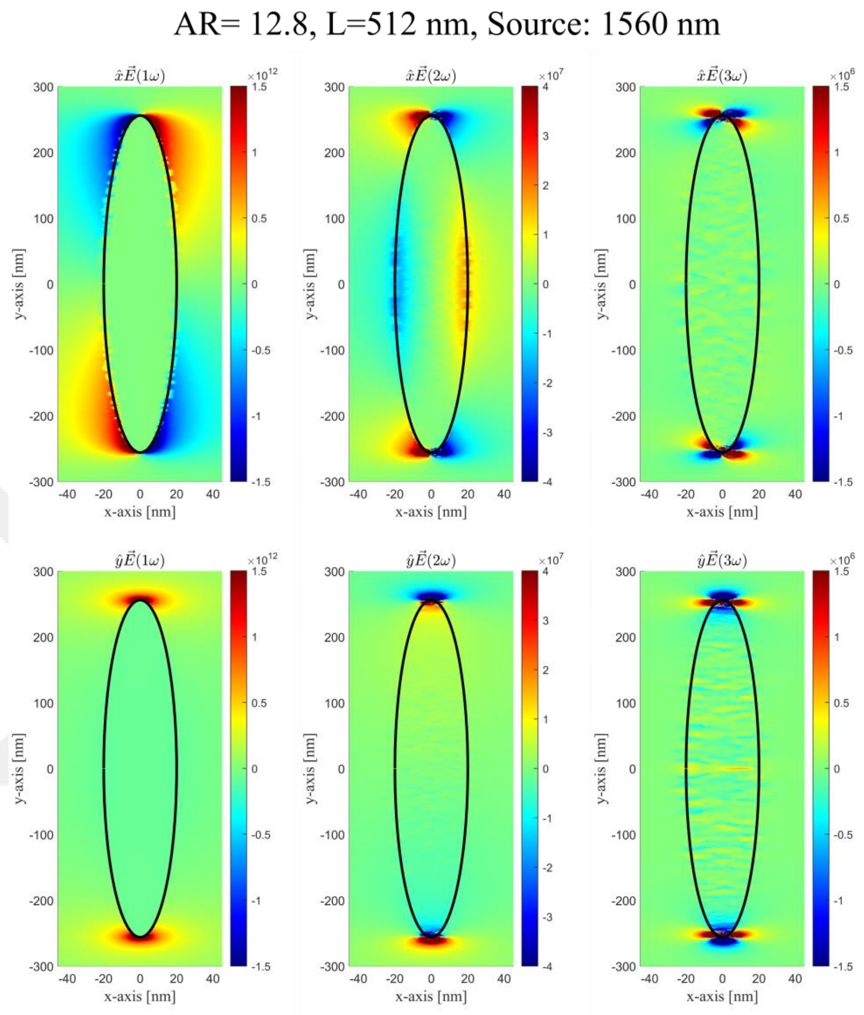

Figure 2.1.2: Plots of near-fields for orders 1-3 and polarizations x and y. The electric fields are the complete form of Figure 2.1.1. Standard smoothing is removed, showing meshing artifacts at lower intensities, especially for third harmonic generation.

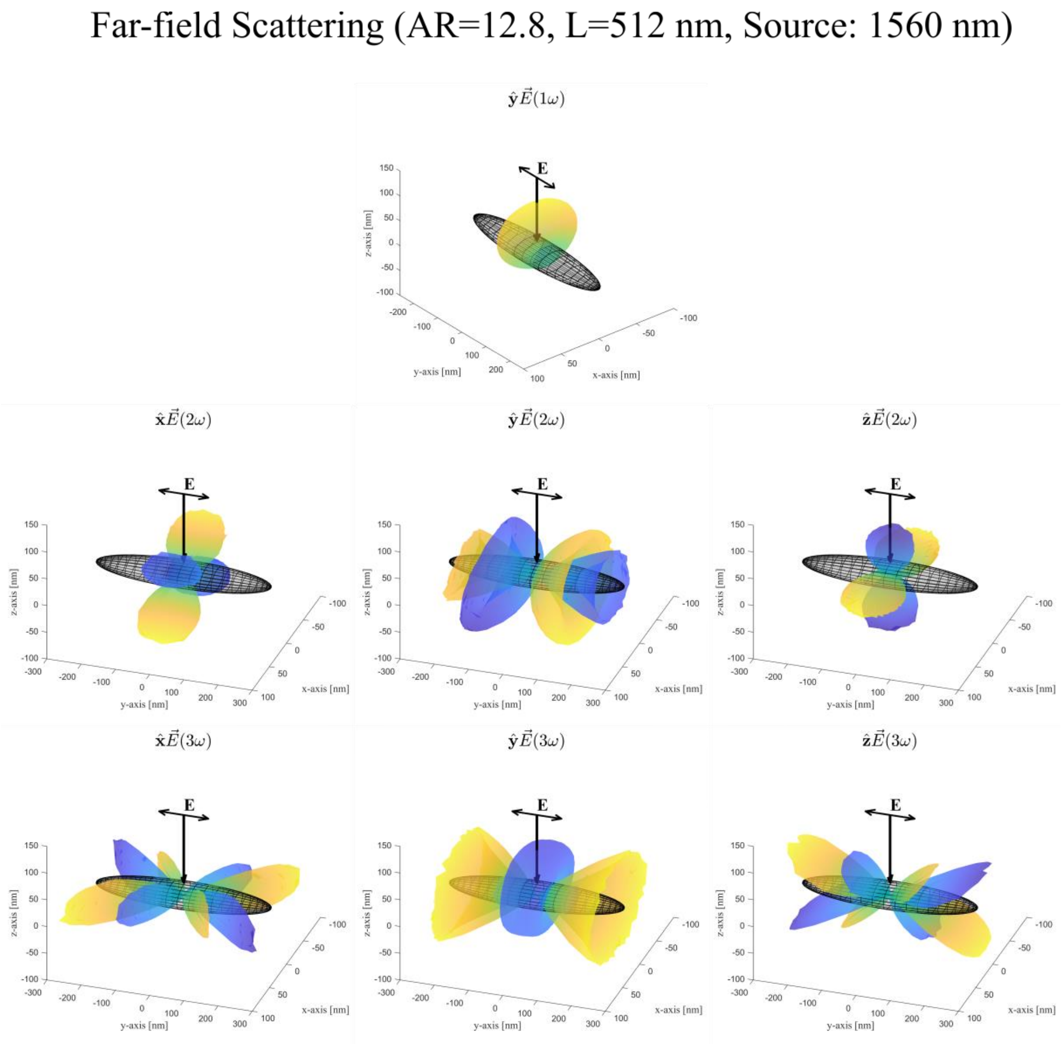

Figure 2.1.3: Far-fields are measured from an outer ellipsoid surface distanced half a wavelength from the outer surface of the gold ellipsoid. The gold ellipsoid domain is subject to Navier-Stokes' equation and, as seen in Figure 2.1.2, has near-fields in the form of spherical harmonics. The air domain is only subject to the source-free Maxwell's equations, and vector spherical harmonics are expected, similar to Mie theory. The scattered far-fields are plotted for different polarizations and consist of vector spherical harmonics.

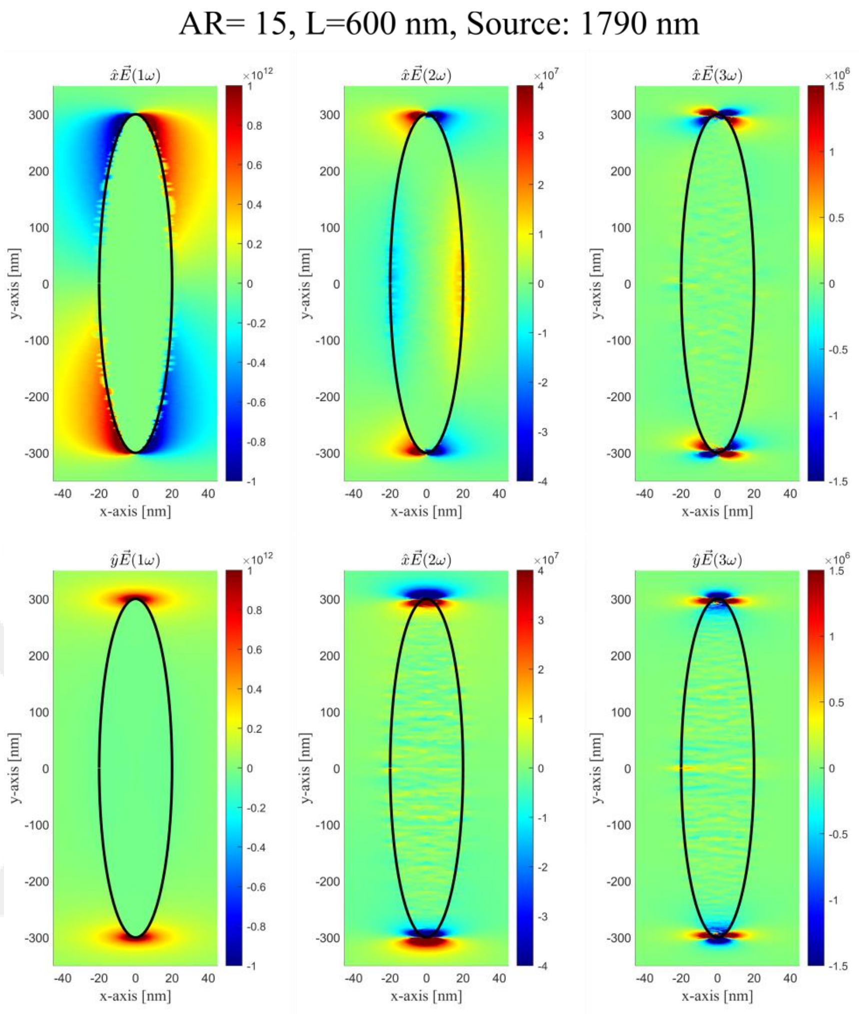

Figure 2.1.4: Near-fields for Larger Aspect Ratio Particle. The spherical harmonics of a nanoellipsoid with a larger aspect ratio is near identical to the spherical harmonics in Figure 2.1.2. The diameter is 20 nm and the height is 600 nm. Incident wavelength is adjusted to 1790 nm.

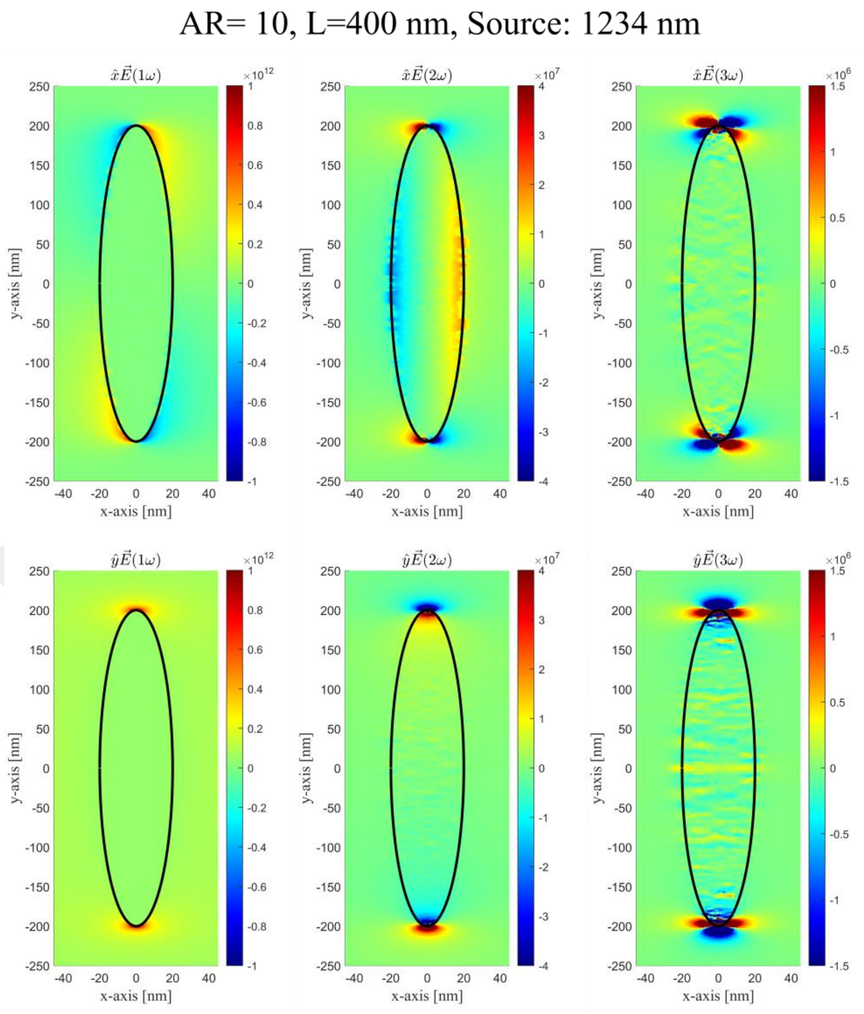

Figure 2.1.5: Near-fields for Smaller Aspect Ratio Particle. The spherical harmonics of a nanoellipsoid with a larger aspect ratio is near identical to the spherical harmonics in Figure 2.1.2. The diameter is 20 nm and the height is 400 nm. Incident wavelength is adjusted to 1234 nm.

2.2 Sharp , Regular, Blunt and Flanged Nanorods

In addition to nano ellipsoids, nanorods with sharp, blunt, and flanged tips are simulated. Figure 2.2.1 shows the shapes and dimensions of the nanorods. The rods were optimized to absorb a wavelength of 1560 nm and polarized along the long-axis of the nanorod. Sharper tips require longer rods, and blunter/flanged tips lead to shorter rods. Figure 2.2.2 plots the electric fields of the sharp-tipped nanorod. The electric fields are stronger than nanoellipsoids and the other simulated types of nanorods. Figures 2.2.3-2.2.5 plot the electric fields of regular, blunted, and flanged tips, which overall have significantly weaker second harmonics compared to sharp tips. Regular. Blunted and flanged nanorods have their third harmonics below the noise floor and are not shown in Figures 2.2.3-2.2.5. On close inspection of Figures 2.2.3-2.2.5, one can observe the formation of electric fields and spherical harmonics on corners and edges where the cones at the tips are connected to the cylindrical body.

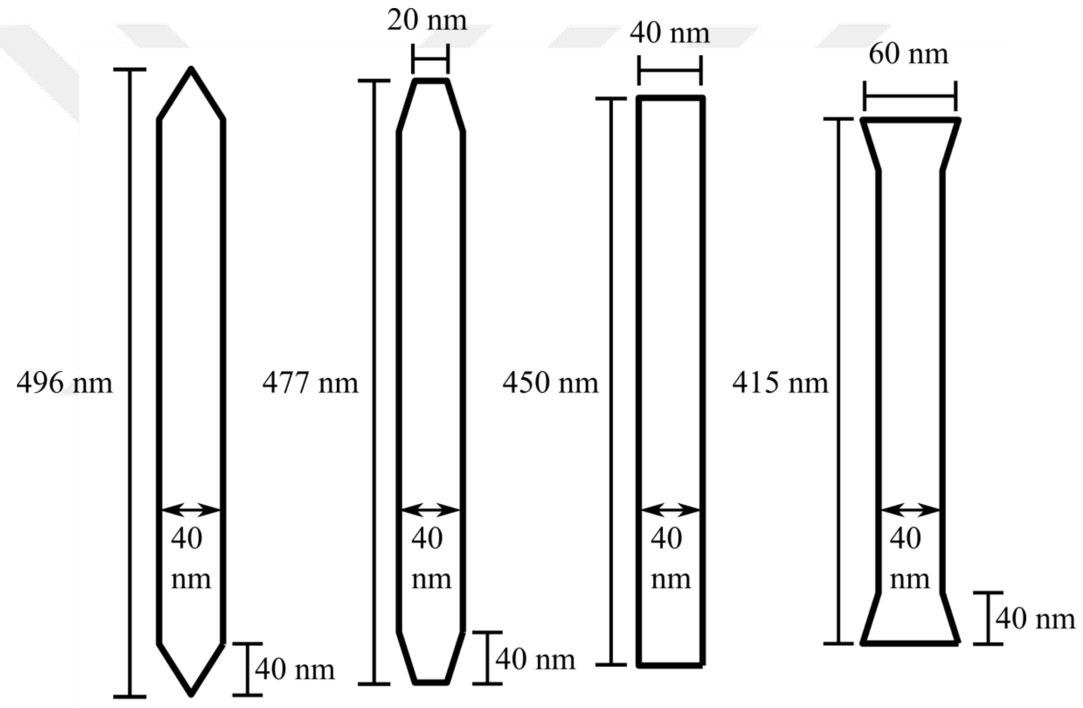

Figure 2.2.1: Dimensions of Nanorods. Dimensions of four nanorods with varying levels of tip sharpnesses. The tip radii 0, 20, 40 and 60 nm. All nanorods have identical absorption peaks at 1560 nm. Sharper tipped nanorods are longer and blunter tips are shorter.

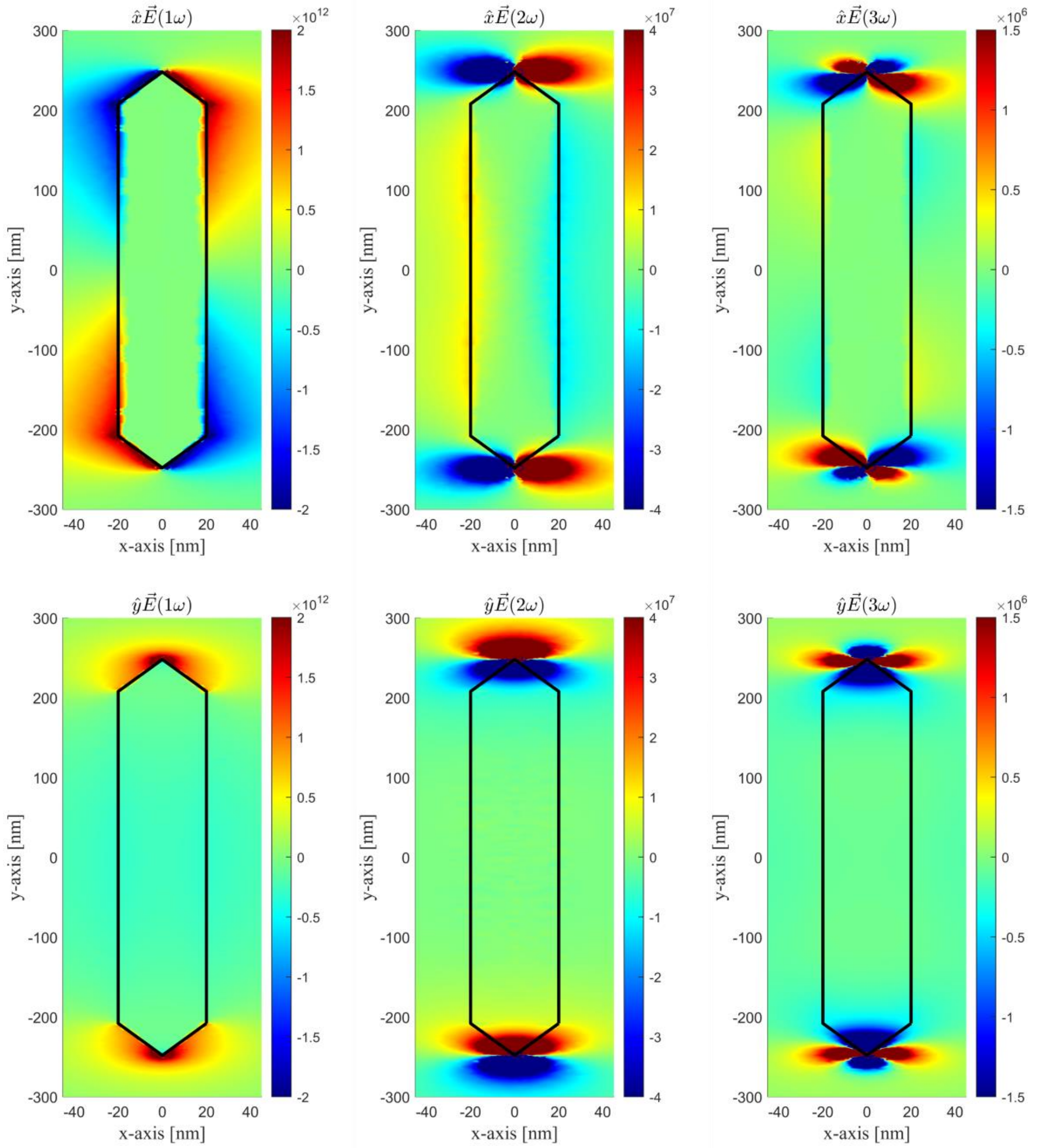

Figure 2.2.2: Near-fields for Sharp Tipped Rods. The electric fields and the spherical harmonics of sharp tips are stronger compared to ellipsoids and rods with blunter tips.

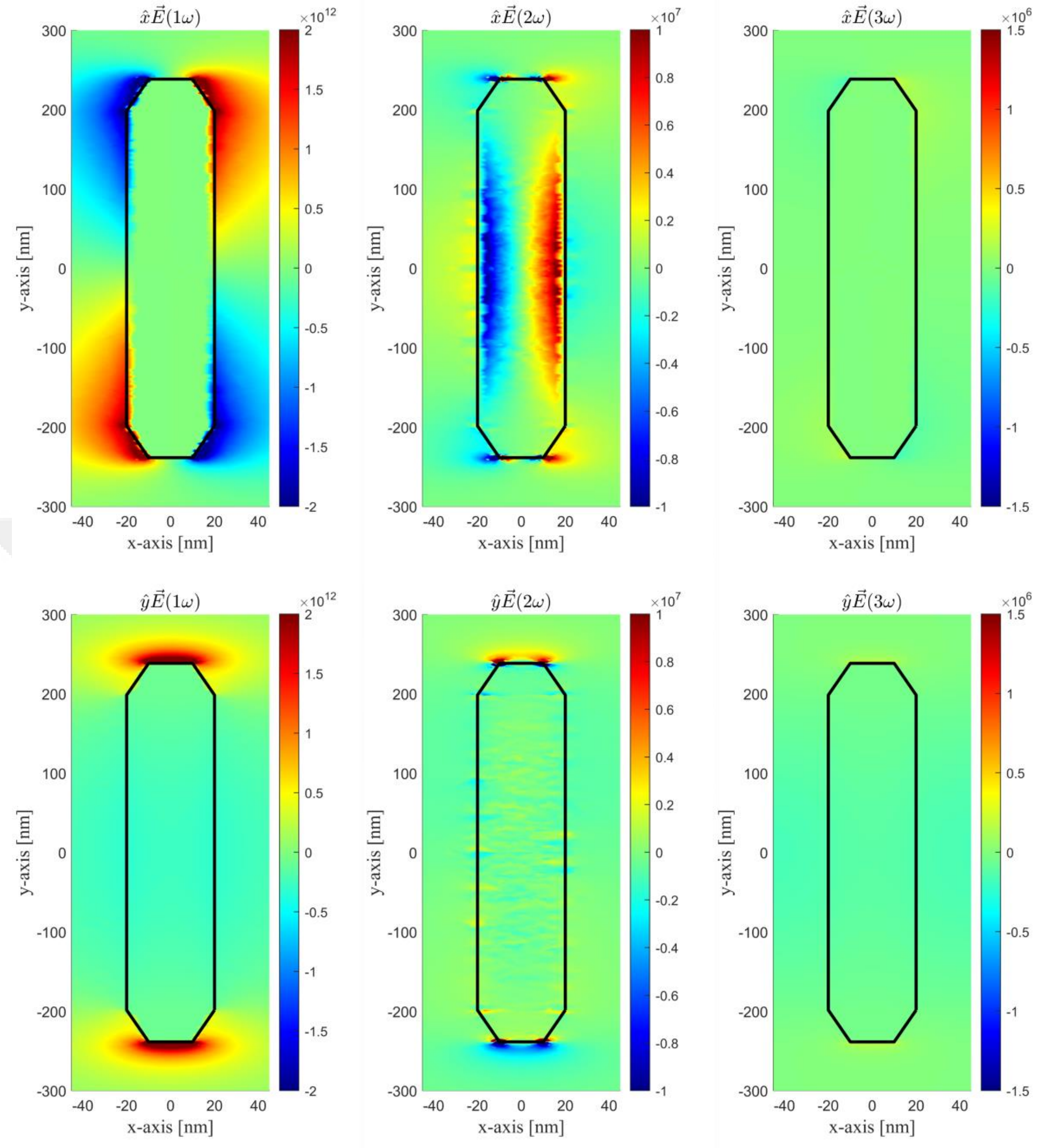

Figure 2.2.3: Near-fields for Rod with Tip Diameter of 20 nm. The electric fields and the spherical harmonics are significantly weaker compared to sharp tips or ellipsoids. Third harmonics do not exist due to the low amplitudes.

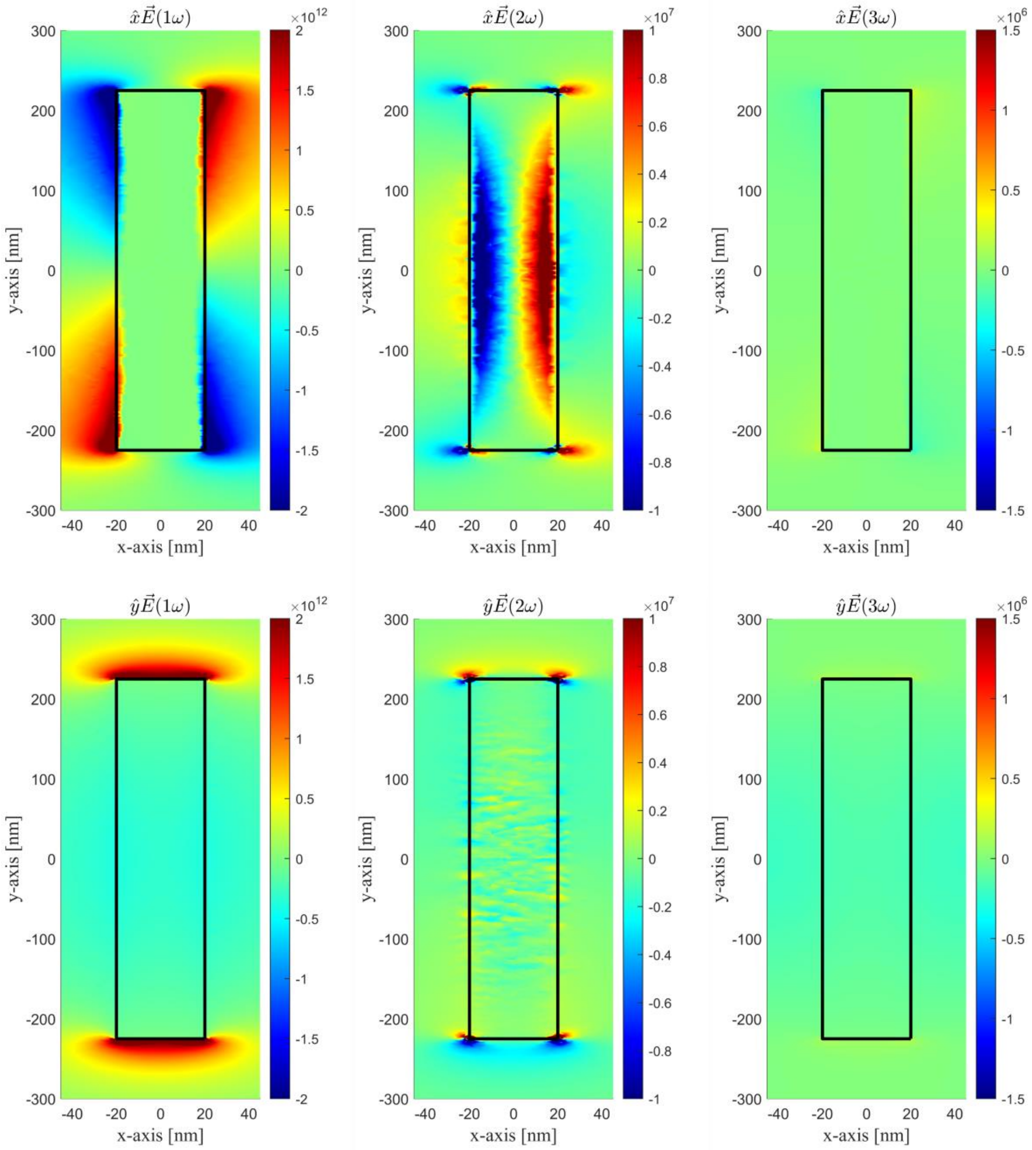

Figure 2.2.4: Near-fields for a Regular Rod with Tip Diameter of 40 nm. The electric fields and the spherical harmonics are significantly weaker compared to sharp tips or ellipsoids. Third harmonics do not exist due to the low amplitudes.

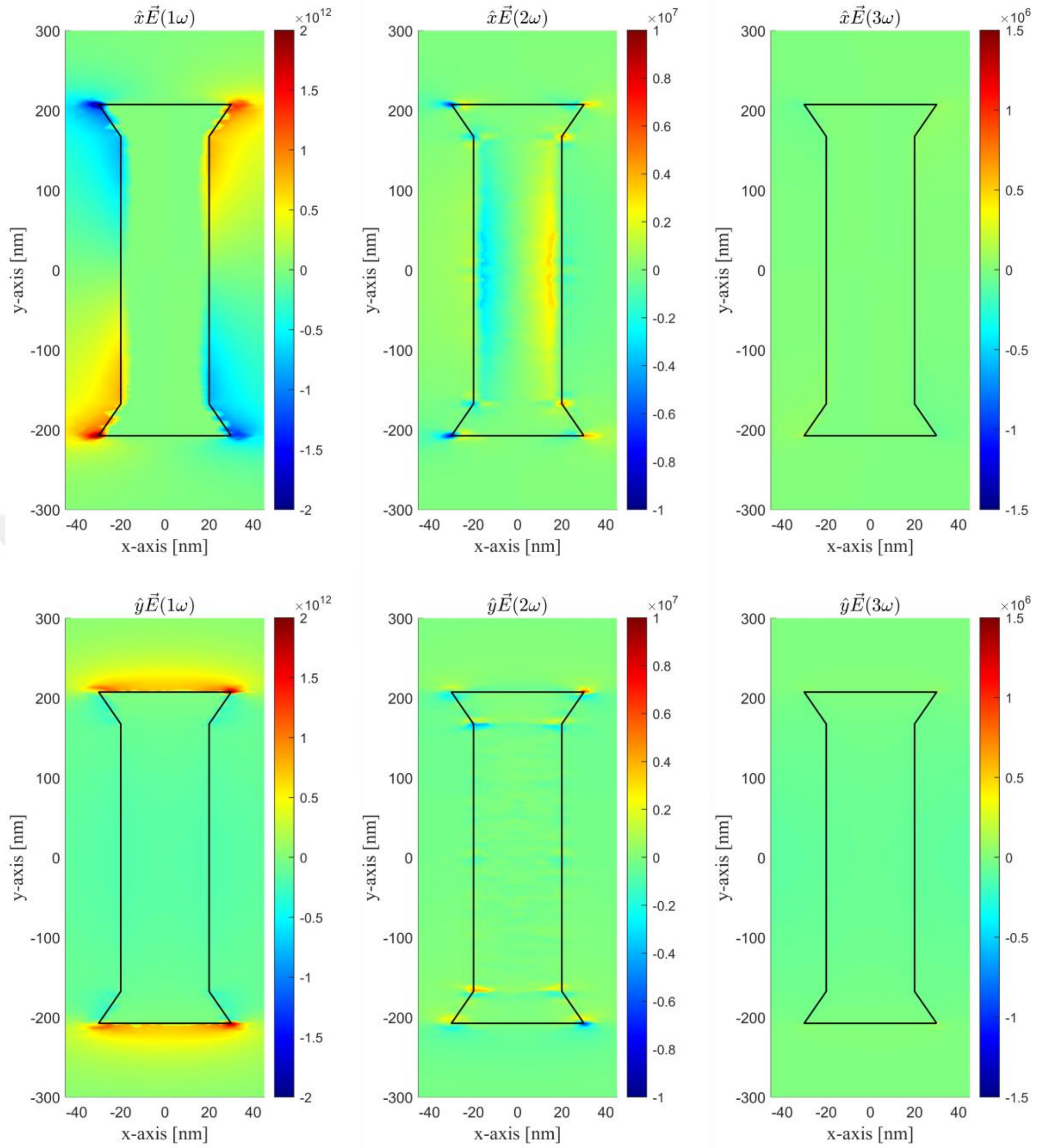

Figure 2.2.5: Near-fields for Rod with Tip Diameter of 60 nm. The electric fields and the spherical harmonics are the weakest of the simulated rods. The first harmonic and second harmonics are weak. Third harmonics do not exist.

CHAPTER 3

SUSCEPTIBILITY MAPS

3.1 Ellipsoids

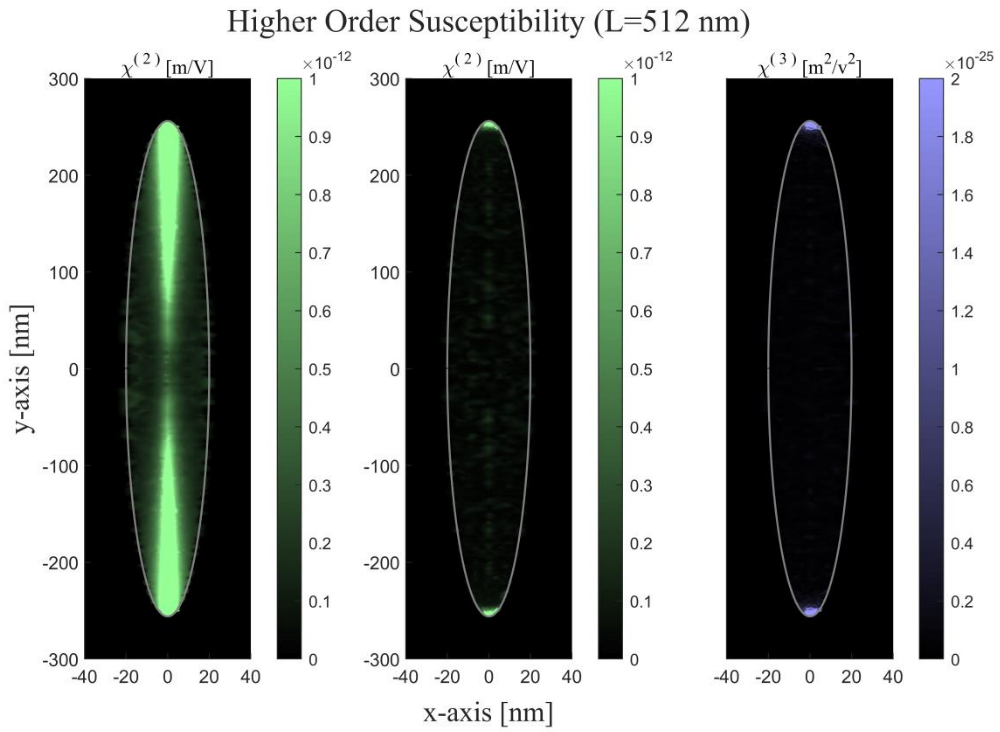

Figure. 3.1.1: Second and third-order polarization-dependent susceptibility maps.

Extracting higher order susceptibility maps (especially second order maps) from the hydrodynamic simulations are important because gold has a centro-symmetric lattice and does not support SHG. The maps in Figure 3.1.1 explain particle shape and size effects on the generation of second harmonics. The higher-order susceptibility maps are calculated using the following equations in the post-process, revealing where the second and third harmonic generation occur.

$$P_i(2\omega) = \epsilon_0 \sum_{jk} \chi_{ijk}^{(2)} E_j(\omega) E_k(\omega) \quad (3.1.1)$$

$$P_i(3\omega) = \epsilon_0 \sum_{jkl} \chi_{ijkl}^{(3)} E_j(\omega) E_k(\omega) E_l(\omega) \quad (3.1.2)$$

Equation 1.6.5 gives the anisotropic and time-dependent polarization density. Values of $P_i(2\omega)$ and $P_i(3\omega)$ are determined by performing a fast Fourier transform (FFT) on $\vec{P}(t)$. Values of $E_i(\omega)$ are found using the same method as for the polarization density.

Figure 3.1.1 shows the higher-order susceptibility mapping results for both incident polarizations. The peak susceptibility values in Figure 3.1.1 are $\chi_{y-pol}^{(2)} = 3.4 \cdot 10^{-12}\, m/V$, $\chi_{x-pol}^{(2)} = 5.5 \cdot 10^{-12}\, m/V$ and $\chi_{y-pol}^{(3)} = 1.8 \cdot 10^{-24}\, m^2/V^2$. All maximum susceptibility values are located at the ellipsoid tips, especially for the y-polarized source. The average values are given in Table 3.2.1. However electric fields are mainly located at the tips of the nanoellipsoids, which makes the maximum susceptibility values at the particle tips more relevant compared to the averaged values.

A x-polarized source is ttested, producing a second-order susceptibility map with values extending further into the nano-ellipsoid. The third-order susceptibility during x-polarized excitation is omitted due to low amplitude. The amplitude of the third harmonic generation under x-polarized excitation is below the noise level, which is expected because the long axis of the gold ellipsoid (y-polarization) is only resonant for 1560 nm wavelength. Polarization along the short axis severely dampens the peak amplitudes of all harmonics, shown in the polarization-dependent spectra in Figure 5.3.

Figures 3.1.2 and 3.1.3 add the susceptibility maps of two additional aspect ratios. The longer nanoellipsoid was illuminated with a 1790 nm source and has the highest second and third-order susceptibility values among the three nanoellipsoids. The shorter nanoellipsoid is the weakest and was illuminated with a 1234 nm source.

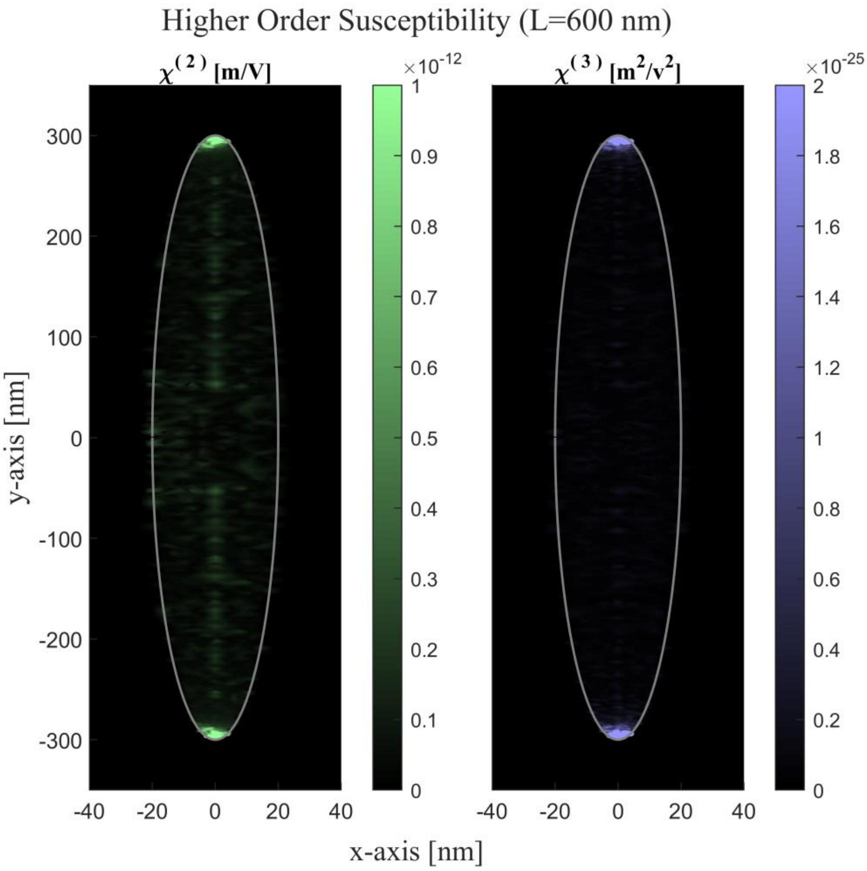

Figure. 3.1.2: Second and Third-Order Susceptibility of a Long Nano Ellipsoid. The length of the nanoellipsoid is increased to 600 nm, which shifted the long-axis resonance to 1790 nm.

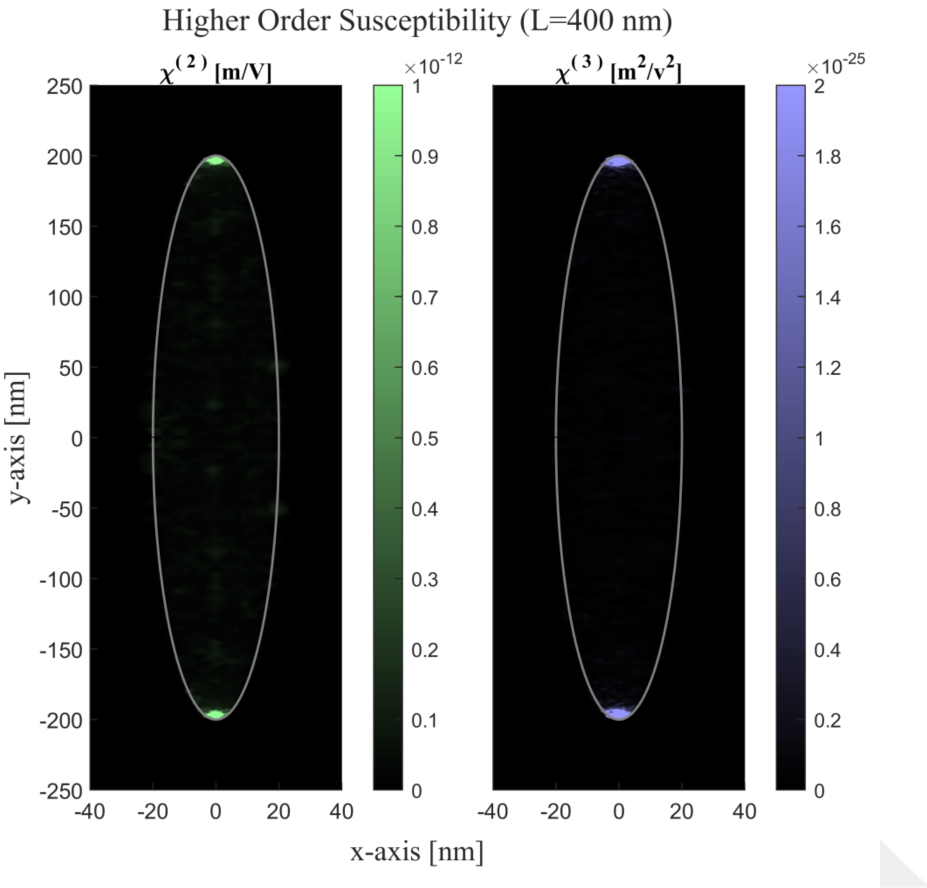

Figure. 3.1.3: Second and Third-Order Susceptibility of a Short Nano Ellipsoid. The length of the nanoellipsoid is increased to 400 nm, which shifted the long-axis resonance to 1234 nm.

The third-order value in Figure 3.1.1 is compared with Equation 3.1.10, giving an expected dipole approximated third-order susceptibility value of $\chi^{(3)}_{dipole} = 1.4 \cdot 10^{-24}\ m^2/V^2$ for a gold nanosphere (r=256 nm), in agreement with the simulated third-order susceptibility value. The expected dipole value is calculated as follows:

Kerr susceptibility for a dipole is approximately given by [28]:

$$\chi^{(3)}_{intra}(\omega, -\omega, \omega) = -i\frac{64}{45\pi^2}T_1T_2\frac{1}{a^3}\frac{e^4}{m^2\hbar^5\omega^7}E_F^4 g_1(\nu)(1 - a/a_0) \qquad (3.1.3)$$

, where $T_1 = 5 \cdot 10^{-13}\ s$ is energy lifetime, $T_2 = 5 \cdot 10^{-14}\ s$ is de-phasing time, $\nu = \hbar\omega/E_F$, a=256 nm is the particle radius and $E_F = 5.5\ eV$ (gold).

$$a_0 = T_2\sqrt{\frac{2E_F}{m}}g_1(\nu)[g_2(\nu) + g_3(\nu)] \tag{3.1.4}$$

For $\lambda = 1560\ nm$ or $\omega = 1.21 \cdot 10^{15}\ rad/s$:

$$g_1(\nu) = \frac{1}{\nu}\int_{1-\nu}^{1} x^{5/2}(x+\nu)^{3/2}dx \tag{3.1.5}$$

$$g_2(\nu) = \frac{1}{\nu}\int_{1-\nu}^{1} x^{3/2}(x+2\nu)^{1/2}dx \tag{3.1.6}$$

$$g_3(\nu) = \frac{1}{\nu}\int_{max(\nu,1-\nu)}^{1} x^{5/2}(x+\nu)^{1/2}(x-\nu)^{1/2}dx \tag{3.1.7}$$

Here calculated values are $g_1(\nu) = 0.931$, $g_2(\nu) = 1.102$, $g_3(\nu) = 0.768$, and $a_0 = 86.5\ nm$. Kerr susceptibility is calculated:

$$\left|\chi_{intra}^{(3)}(\omega,-\omega,\omega)\right| \simeq 1.407 \cdot 10^{-20}\ [m^2/\,V^2] \tag{3.1.8}$$

, and is related to third harmonic susceptibility by a factor of four orders of magnitude [29],

$$\left|\chi_{intra}^{(3)}(\omega,-\omega,\omega)\right| / \left|\chi_{intra}^{(3)}(\omega,\omega,\omega)\right| \sim 10^4 \tag{3.1.9}$$

Finally, the dipole approximation of third harmonic susceptibility has the value:

$$\left|\chi_{intra}^{(3)}(\omega,\omega,\omega)\right| \simeq 1.4 \cdot 10^{-24}\ [m^2/\,V^2] \tag{3.1.10}$$

3.2 Sharp, Regular, Blunt and Flanged Nanorods

Increasing the particle surface area increases the second-order susceptibility tensors [30, 31]. The effect of corner sharpness has also been studied experimentally [32]. Here, nanorods with different tips are simulated, and their higher-order susceptibility maps are plotted. Figure 3.2.1 shows that the sharp-tipped nanorod has the highest susceptibility values. The remaining rods with blunt, regular, and flanged tips have weaker second-order susceptibilities (Figure 3.2.2) and do not have any significant third-order susceptibility (the third harmonic electric fields are below the noise floor).

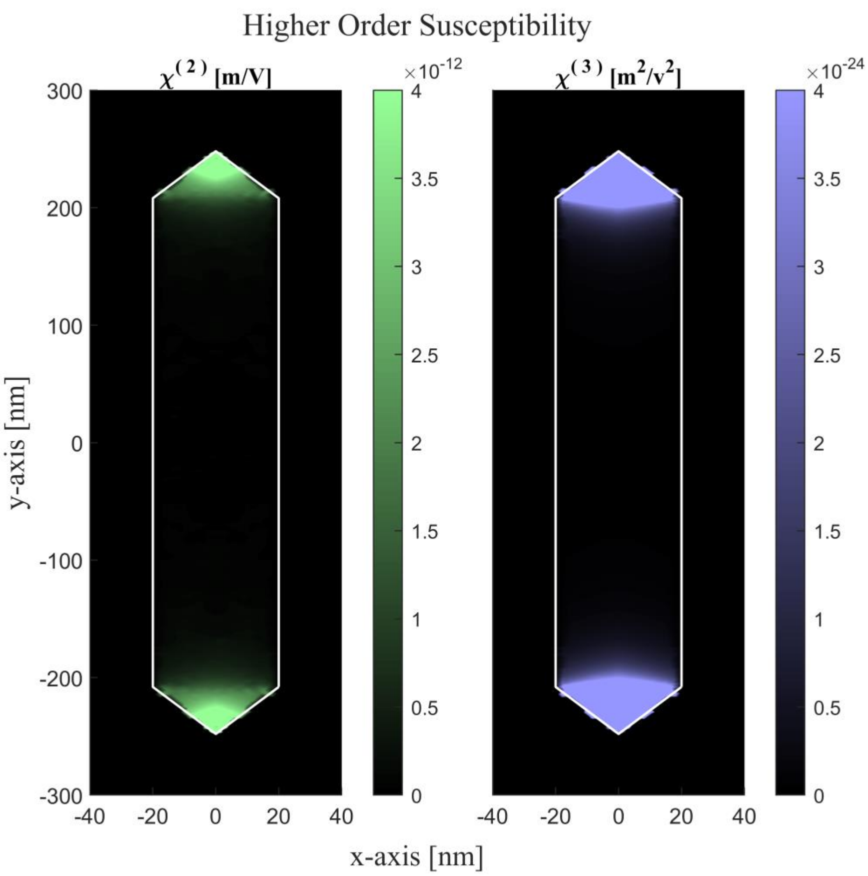

Figure. 3.2.1: Second and Third-Order Susceptibility of a Sharp Tipped Nanorod. The long-axis resonance is 1560 nm.

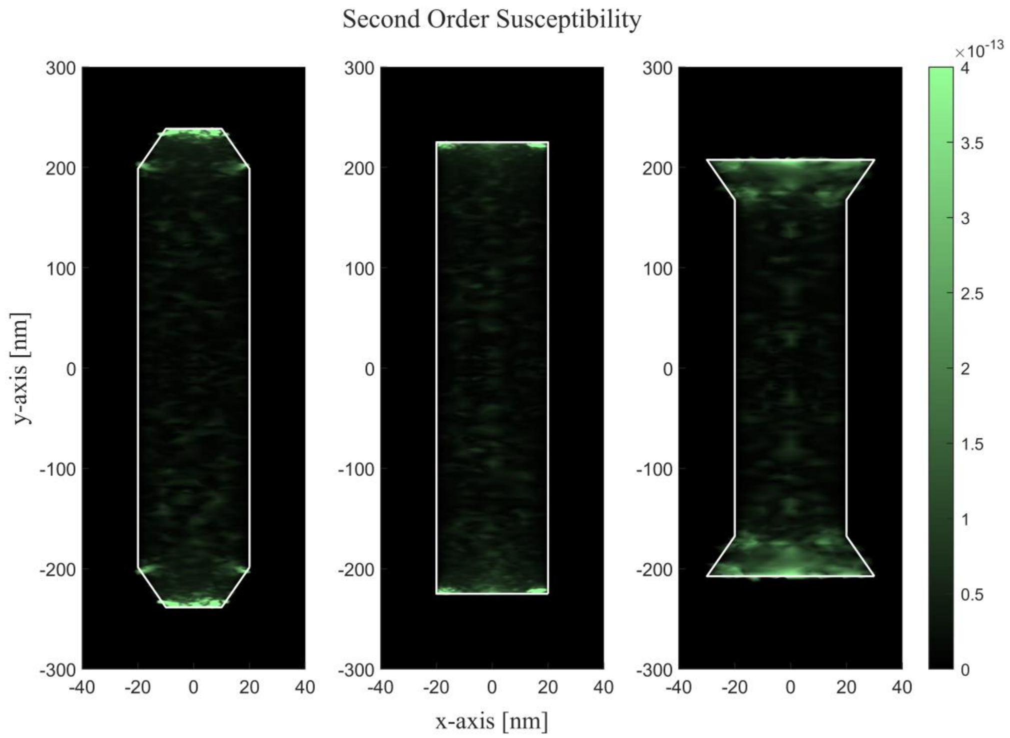

Figure. 3.2.2: Second and Third-Order Susceptibility of a Blunted, Regular and Flanged Nanorod. All rods have their long-axis resonance at 1560 nm. Un-sharp tips all have low second susceptibilities. Third harmonics are below the noise floor and does not exist (Figures 2.2.2-2.2.5 show non-existent third harmonics.)

3.3 Comparison and Discussion

Several authors have conducted studies analyzing the effects of particle shape and size on second-order hyperpolarizabilities, which is closely related to the second-order susceptibility tensor. Ledoux-Rak et al. [31] and Chandra et al. [30] have found that the nanorod surface area is the dominant factor determining the hyperpolarizability, not the aspect ratio. Chandra et al. [30] studied samples of closely packed gold nanorods with similar aspect ratios and concluded that the hyperpolarizability is linearly dependent on particle surface area. Ledoux-Rak et al. [31] studied samples of separated nanospheres and rods with considerably lower particle concentrations compared to Chandra et al. Results of Ledoux-Rak et al. show that spheres have a linear dependency on surface area. However, isolated nanorods show nonlinear hyperpolarizability to surface area dependency. Curve fitting the results of Ledoux-Rak et al. show a nonlinear surface area relation proportional to the power of 4.6. Ledoux-Rak et al. adjusted two axes of the nanorods when changing their dimensions, meaning the surface area was increased quadratically between the four samples. Second-order polarizability increases quadratically with increasing input intensity. The expected hyperpolarizability to surface relation should be proportional to the power of 4.

The simulated second-order susceptibilities for all types of rods are tabulated in Table 3.2.1, which shows two trends. An increase in particle size and sharper tips increase the second-order susceptibility values. The second-order susceptibility values for the three ellipsoids depend on the surface area by the power of 2.03. The ellipsoids were only elongated along a single axis. Therefore, the surface area, volume, and absorption cross-section increase linearly. A linear increase in electron velocity would lead to an expected quadratic polarizability increase.

In a later article, Ledoux-Rak et al. [32] also studied the corner sharpness of nano prisms. An increase in corner sharpness led to an increase in hyperpolarizability. The prisms were tightly packed, and the hyperpolarizability was linearly dependent on surface area. Tightly packed samples likely exhibit linear surface area to hyperpolarizability relations, whereas isolated particles are nonlinearly dependent on surface area.

Table. 3.2.1: Maximum and Average Second Order Susceptibility Values.

Type of Nanorod	Maximum	Average
Ellipsoid (L=400 nm)	$3.00 \cdot 10^{-12}\ m/V$	$2.12 \cdot 10^{-14}\ m/V$
Ellipsoid (L=512 nm)	$3.40 \cdot 10^{-12}\ m/V$	$2.55 \cdot 10^{-14}\ m/V$
Ellipsoid (L=600 nm)	$6.04 \cdot 10^{-12}\ m/V$	$4.30 \cdot 10^{-14}\ m/V$
Sharp Tip	$1.78 \cdot 10^{-11}\ m/V$	$4.03 \cdot 10^{-13}\ m/V$
Blunted Tip	$2.45 \cdot 10^{-12}\ m/V$	$2.02 \cdot 10^{-14}\ m/V$
Cylindrical Rod	$1.03 \cdot 10^{-12}\ m/V$	$1.80 \cdot 10^{-14}\ m/V$
Flanged Tip	$5.15 \cdot 10^{-13}\ m/V$	$1.72 \cdot 10^{-14}\ m/V$

Table. 3.2.2: Volume and Surface Area Values of the Different Types of Rods.

Type of Nanorod	Volume	Surface Area
Ellipsoid (L=400 nm)	$3.35 \cdot 10^{5}\ nm^{3}$	$3.93 \cdot 10^{4}\ nm^{2}$
Ellipsoid (L=512 nm)	$4.29 \cdot 10^{5}\ nm^{3}$	$5.03 \cdot 10^{4}\ nm^{2}$
Ellipsoid (L=600 nm)	$5.03 \cdot 10^{5}\ nm^{3}$	$5.88 \cdot 10^{4}\ nm^{2}$
Sharp Tip	$5.56 \cdot 10^{5}\ nm^{3}$	$5.79 \cdot 10^{4}\ nm^{2}$
Blunted Tip	$5.58 \cdot 10^{5}\ nm^{3}$	$5.83 \cdot 10^{4}\ nm^{2}$
Cylindrical Rod	$5.66 \cdot 10^{5}\ nm^{3}$	$5.91 \cdot 10^{4}\ nm^{2}$
Flanged Tip	$5.17 \cdot 10^{5}\ nm^{3}$	$6.02 \cdot 10^{4}\ nm^{2}$

CHAPTER 4

COMPARISON WITH DRUDE MODEL

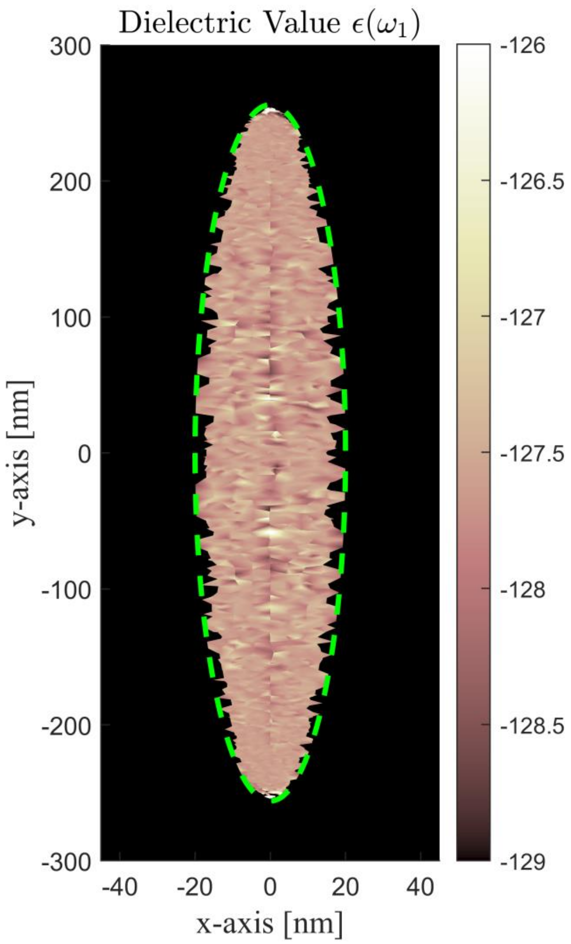

Figure 4.1: Spatial Map of the Dielectric Function at 1560 nm Wavelength: The average dielectric value equals -127.6, close to the theoretical value of -127.1 (stemming from the Drude model).

The Navier-Stokes' equation in Equation 1.6.2 is similar to the free electron Drude model. The main difference is the absence of the non-linear term in the Drude model. The non-linear term grows in amplitude at larger intensities, meaning the Navier-Stokes equation should equal the Drude model at lower intensities. A comparison can be performed by studying the dielectric values at the fundamental frequency of 1560 nm. The frequency-dependent Drude dielectric function is given by the expression:

$$\epsilon(\omega) = 1 - \frac{ne^2}{\epsilon_0 m \omega^2} \tag{4.1}$$

, which gives a value of -127.1 at 1560 nm wavelength. The spatial dielectric map in Figure 4.1 was plotted using the following expression:

$$\epsilon = 1 + \frac{\vec{P}}{\epsilon_0 \vec{E}} \tag{4.2}$$

The maximum and minimum values were -102.7 and -135.2, respectively. Figure 4.1 is noticeably noisy in the middle part but has noise-less values at the nanoellipsoid tips. The reason is the use of a mesh of different sizes. The advantage of the Finite Element Method is the ability to use fine mesh in areas where intense fields are expected and coarser mesh in less critical areas. Figures in Chapters 2 and 3 show that the electric fields are confined to the tips of the nanorods.

CHAPTER 5

SPECTRA AND POLARIZATION DEPENDENCY

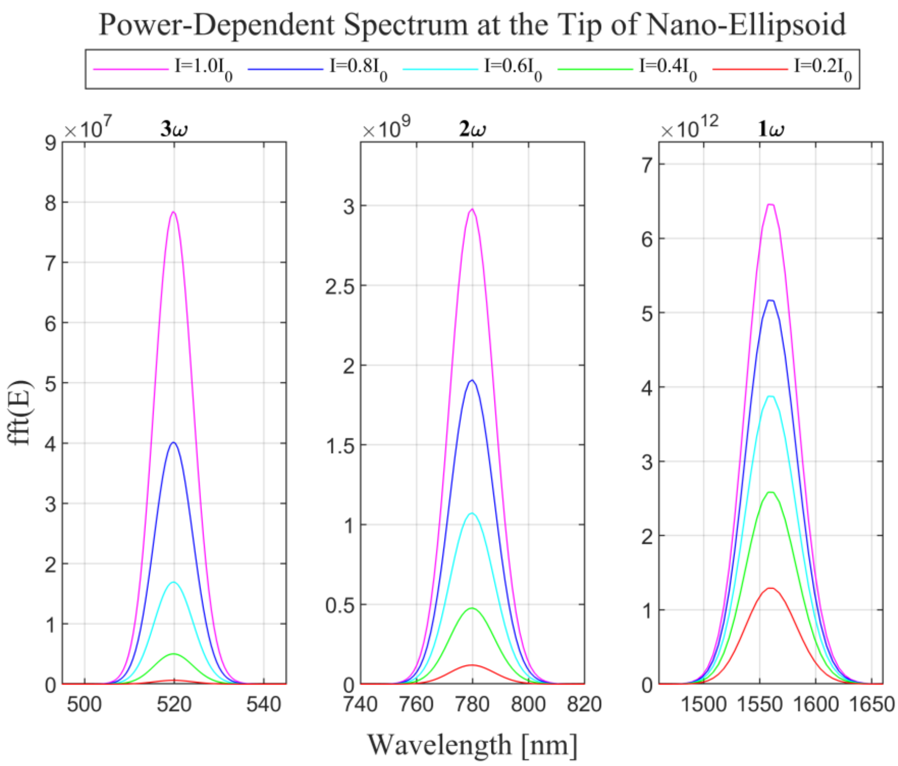

Figure 5.1: Power-Dependent Spectra. Power-dependent spectrum on the tip of the gold nano-ellipsoid.

Figure 5.1 shows the incident power-dependent spectra of the gold nano-ellipsoid. Different input intensities are tested, and the second and third harmonic generation increases quadratically and cubically with increasing input power, respectively (Figure 5.2 plots the SHG and THG intensity values.). Full width at half maximum (FWHM) values are 53.2 nm (fundamental wavelength), 18.7 nm (second harmonic), and 10.2 nm (third harmonic).

The expected FWHM values are calculated using the following expressions:

$$e^{-Nat^2} = 1/2 \tag{5.1}$$

$$\tau = 2\sqrt{\ln(2)}\,/\sqrt{N \cdot a} \tag{5.2}$$

$$\tau = 0.441/\Delta\nu \tag{5.3}$$

Equation 5.1 expresses the time-values t where the pulse-value is half, and N is the N:th harmonic. Equation 5.2 gives the pulse length τ, which is simply two times the solution of Equation 5.1. Equation 5.3 converts simulated spectral bandwidths to pulse lengths, where $\Delta\nu$ is the spectral bandwidth in Hz. The factor of 0.441 is the time-bandwidth product for a Gaussian pulse.

Using Equation 5.3, pulse lengths for the fundamental, second, and third harmonic are 67.3 fs, 47.8 fs, and 39.0 fs, respectively. Expected theoretical pulse lengths according to Equation 35 are 67.2 fs, 47.8 fs, and 39.0 fs, respectively. Expectedly, higher harmonic generation produces ultrashort and wide bandwidth pulses [33]. The nonlinear terms in Equation 1.6.2 facilitate the multiplication of two fields, which results in the second and third harmonic generation. Third harmonic generation is a process where three photons at the fundamental wavelength are combined to create a photon with triple the energy. Third harmonic generation is not directly enabled in Equation 1.6.2 (Navier-Stokes equation). In the initial step, second harmonic generation is created by multiplying two fields at the fundamental frequency. In the subsequent step, a second harmonic wave is combined with a fundamental frequency to create the third harmonic. Fourth harmonics are likewise created by combining two second-order harmonics. However, the use of gold limits the fourth harmonics during 1560 nm wavelength illumination due to its plasmon resonance frequency. Using silver instead of gold would allow the fourth harmonic generation at 390 nm.

The nanoellipsoid has two axes, and the excitation along the long axis corresponds to a 1560 nm wavelength peak. Using the same 1560 nm wavelength, excitation along the short axis results in drastically reduced SHG and THG values, plotted in

Figure 5.3. THG is reduced, and the peak is below the noise floor, resulting in a noisy peak at 520 nm.

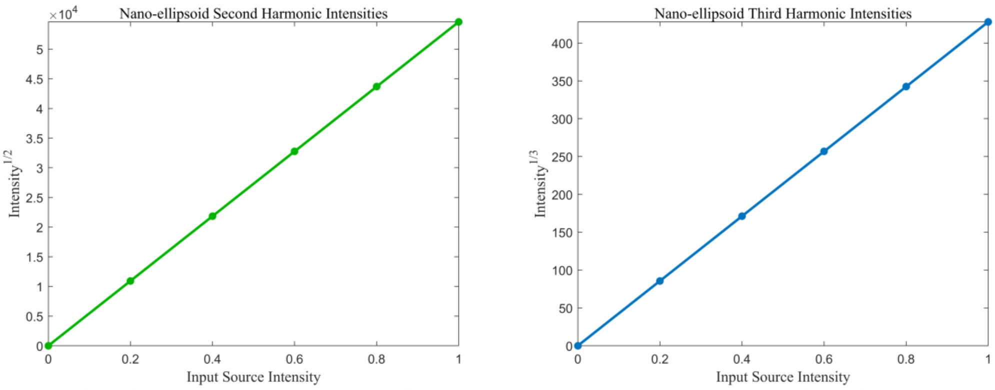

Figure 5.2: Power-dependent second and third harmonic generation. The y-axis of the left and right side plots are square and cube root, respectively. The linear plots means that the second harmonic generation increases quadratically and the third harmonic cubically.

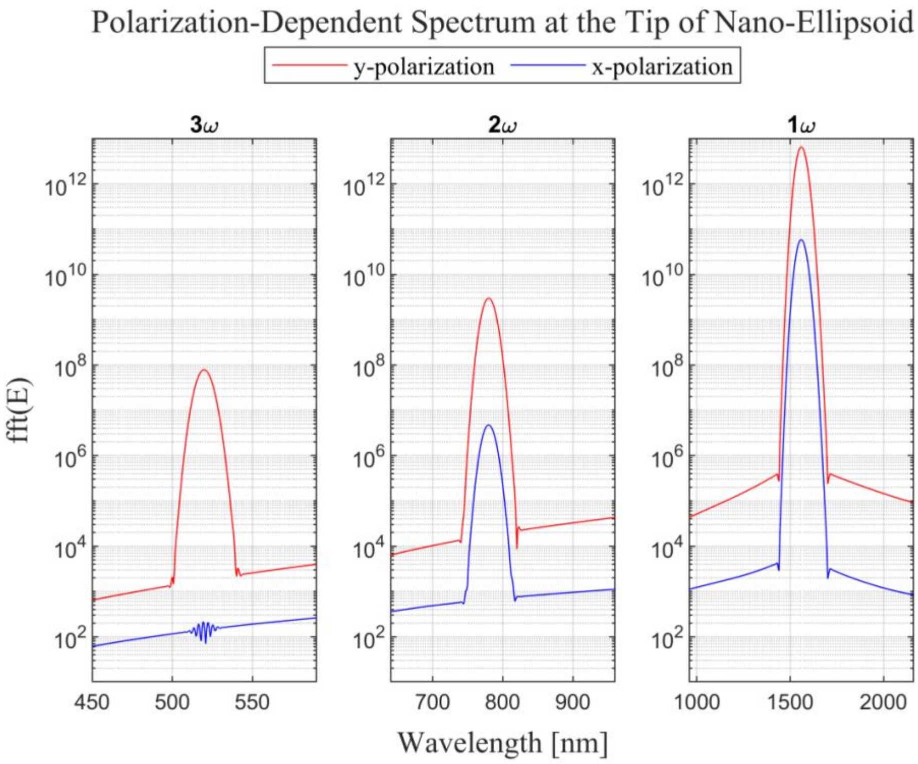

Figure 5.3: Polarization dependent nonlinear spectra. The gold ellipsoid is resonant at 1560 nm in the y-direction. Perpendicular polarization yields a weaker second harmonic generation, and the third harmonic generation is under the noise floor.

CHAPTER 6

WAVE-MIXING

6.1 Four and Five Wave Mixing

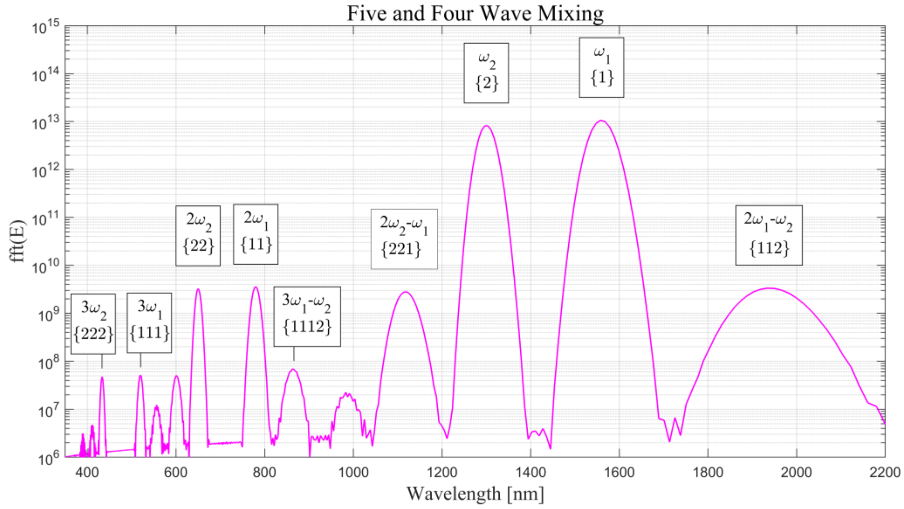

Figure. 6.1.1: Spectra of Four and Five Wave Mixing. Two fundamental input wavelengths are 1300 and 1560 nm. Second and third harmonics are mixed with the fundamental wavelengths to create three-, four-, and five-wave mixing. The unmarked peaks belong to the fifth and higher orders of wave mixing.

Wave-mixing is a phenomenon similar to harmonic generation. However, higher harmonics of two or more fundamental frequencies are created and mixed in four-wave mixing. Four-wave mixing is used to entangle photons and has potential uses in quantum information applications [34, 35].

Four and five-wave mixing (4WM & 5WM) is simulated for a gold nano ellipsoid using two standard telecommunication (1300 & 1560 nm) wavelengths at high intensity. Wave mixing is realized through the nonlinear divergence and Lorentz force terms in the Navier-Stokes equation (Equation 1.6.2). The two input sources are directed from two opposite directions into the gold nano ellipsoid ($\vec{E}(\pm\omega_1, \mp\omega_2)$). Equal signs result in sum frequency generation instead of difference frequency generation. The modes in Figure 6.1.1 are indicated by frequency and by braces notation. The total state of the third-order modes for a gold ellipsoid is written in braces notation:

$$\psi_{Au} = \frac{A\{111\}+b\{221\}+b\{112\}}{\sqrt{A^2+2b^2}} \tag{5.1}$$

, where A is the amplitude of the third harmonic and b is the amplitude of the mixed waves (A<b). State ψ_{Au} cannot be factorized due to the different amplitudes; therefore, the third-order states are entangled. In Figure 6.1.1, the similarity in amplitudes of states {221} and {112} are connected to the similarity in the amplitude of the two fundamental frequencies. However, different intensities of the input frequencies would lead to two different values for states {221} and {112}. The state {xxx} is cubically dependent on the input amplitude of {x}, and states {xxy} have a quadratic dependency on {x} and a linear dependency on {y}. Note that the Navier-Stokes equation represents a continuum, not individual particles and their quantum properties. Townsend et al. have used density functional theory to show that single particle and collective dynamics can coexist in gold [36], and Kolwas has calculated coherence times for gold nanoparticles and found them to be on the order of 10^{-13} s [24]. Manipulation of quantum states could be possible at short femtosecond time scales. However, the number of consecutive operations would realistically be limited to tens, or maybe hundreds, of operations before decoherence. The small size of plasmonic nanoparticles, the wide range of frequencies that can be absorbed (VIS-IR), and the absence of phase-matching conditions are advantageous. The simulated conversion efficiencies ($\eta_{4WM} \approx 10^{-6}$ & $\eta_{5WM} \approx 10^{-10}$) of the gold nano ellipsoid compare favorably to semiconductor microrings [34, 35].

The fundamental frequencies and their higher harmonics ({1}, {2}, {11}, {22}, {111} and {222}) are all pure states, see Figure 2.1.1. In Figure 6.1.2, the near-fields of the mixed waves ({221} & {112}) seemingly combine different orders of spherical harmonics. The x-polarized mode at 1115 nm has the clearest combination of pure states (combined first and second-order spherical harmonic).

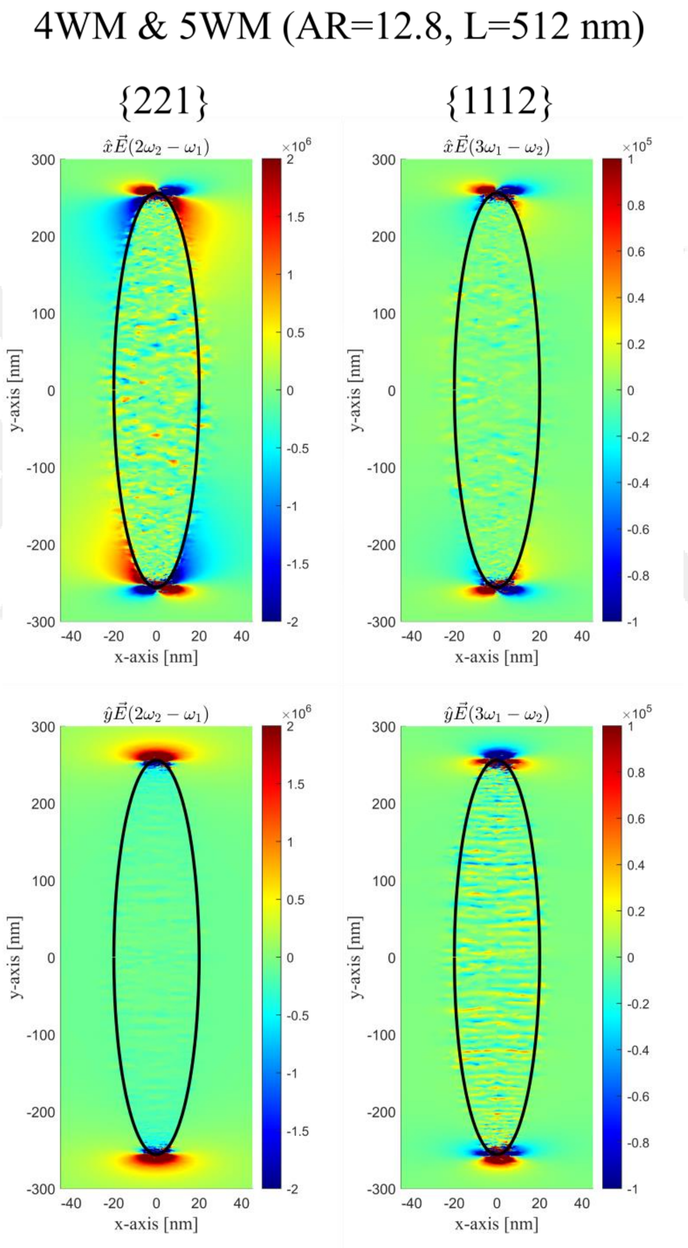

Figure. 6.1.2: Electric Fields of Mixed States. The electric fields of mixed states are combinations of the pure states (Figure 2.1.1).

6.2 Three Wave Mixing

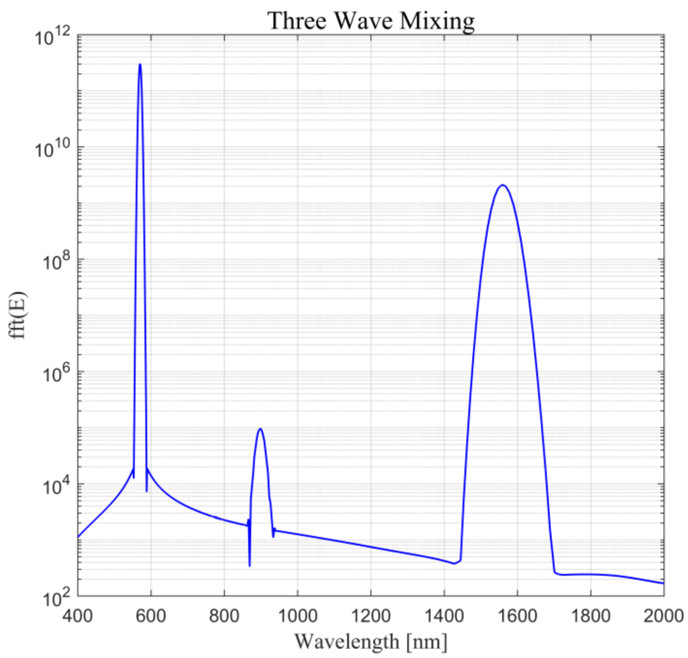

Figure 6.2.1: Three-wave mixing process using a gold nano ellipsoid, where the input signal at 1560 nm is converted to 900 nm using a conceptual 570 nm pump.

Three-wave mixing was studied alongside four and five-wave mixing. Figure 6.2.1 shows the result of a practical conversion concept where a standard telecommunication wavelength at 1560 nm is converted down to 900 nm using a conceptual 570 nm pump. Converting the signal to 900 nm would be advantageous when using silicon photodetectors since 1560 nm photons are not detectable with silicon technology, which has a peak sensitivity at 900 nm wavelength. Pulsed femtosecond lasers are rare, and a 635 nm laser was recently achieved [37]. Although 570 nm femtosecond pulsed lasers do not exist today, shorter wavelength (in the 500 nm range) femtosecond pulsed lasers are expected to be realized in the near future. According to Figure 6.2.1, the 1560 nm pulse was converted to 900 nm. However, the conversion efficiency is not impressive, probably due to mismatching input frequencies and nanoparticle shape. Hybrid particles supporting

570 and 1560 nm pulses would probably achieve significantly higher second order conversion efficiencies.

Difference frequency generation is generally used to convert shorter wavelengths to the infrared and terahertz spectra [38]. Inorganic and organic materials (GaAs, GaSe, GaP and DAST crystal) are used in terahertz (THz) applications. Current sources are bulky and expensive. DFG processes in crystals make miniature and cheap THz sources. However, single crystals have low conversion efficiencies and need to be complemented with waveguides and cavities to increase the nonlinear DFG process.

Lately, quantum information storage has become an important topic. Quantum storage operates in the optical spectrum and needs to be converted to telecommunication wavelengths [39], allowing the linking of separated quantum storages. Afzelius et al. [39] have used a PPLN waveguide's nonlinear properties to convert 580 nm photons efficiently to the 1541 nm telecommunication wavelength via the DFG process.

Afzelius et al. attempted to address the noise during DFG conversion, which they concluded stemmed from the pump laser and spontaneous parametric down-conversion. Lu et al. propose a different but closely related mechanism to decrease noise levels during frequency conversion [40]. The pump laser is not directly fed into the DFG process and is first subject to second harmonic generation (TSFG/TDFG). Lu et al. propose a silicon nitride microring design to convert 606 and 1550 nm wavelengths in both directions.

Other applications include Raman scattering applications [41]. The second-order susceptibility is surface sensitive and independent of glass/silicon substrates. Symmetrical particles exhibit weak second-order optical effects, but symmetry-breaking features such as pillars and tubes exhibit nonlinear properties and have been used to detect thiophenol, which was not detectable using SERS methods.

CHAPTER 7

DIPOLE- AND DOUBLY RESONANT ANTENNAE

The main nanoparticle used in this thesis is the gold nanorod. However, comparing nonlinear simulation results with actual experimental measurements is interesting. Here, the experimental work of Martin [9] was verified by simulating their two types of antennae. Bulk gold only supports THG due to its centro-symmetric lattice. However, metal nanoparticles exhibit SHG, and non-symmetrical shapes further enhance SHG. The two simulated nano-antennae are dipole and doubly resonant antennae. The geometries of both antennae are illustrated in Figure 7.4. The dipole antenna is symmetric and optimized for absorption at 800 nm wavelength. The doubly resonant antenna is optimized for both 400 and 800 nm. The spectra of both antennae under a low-power white light are presented in Figure 7.3. Under intense illumination by an 800 nm pulsed femtosecond laser, the dipole antenna has a much more intense near-field at 800 nm. However, at 400 nm, the SHG of the dipole antenna is much weaker compared to the doubly resonant antenna. Figure 7.2 shows that the doubly resonant antenna has an SHG of more than four times greater than the dipole antenna. The SHG results are interesting because the second harmonic is quadratically dependent on the strength of the fundamental wavelength. The doubly resonant antenna has a weaker near-field at the fundamental wavelength, yet it creates a higher intensity second harmonic generation. The angular scattering spectra of the two antennae are also interesting, as presented in Figure 7.1. The dipole antenna has a symmetrical SHG scattering pattern, and the doubly resonant antenna has a directional scattering lobe.

Compared with the experimental article by Martin, geometrical changes were made for physical reasons. In the experimental case, adhesion layers between the substrate and the antenna may exist. The adhesion material diffuses into the antenna, creating a gradual boundary between the metal and the non-conductive adhesion material [42]. Furthermore, aluminum was used, rapidly forming an oxidation layer. These mentioned boundary effects are very difficult to implement. Therefore, the simulated geometries were adjusted to optimize for 400 and 800 nm wavelengths. The gap sizes and height/widths were kept the same. The input pulses were kept consistent with the input pulses of the gold nano ellipsoid, meaning that the pulselength is shorter than the experiment's. Lastly, in the hydrodynamical simulations, single antennae were simulated, whereas large arrays were used in the experimental work by Martin et al.

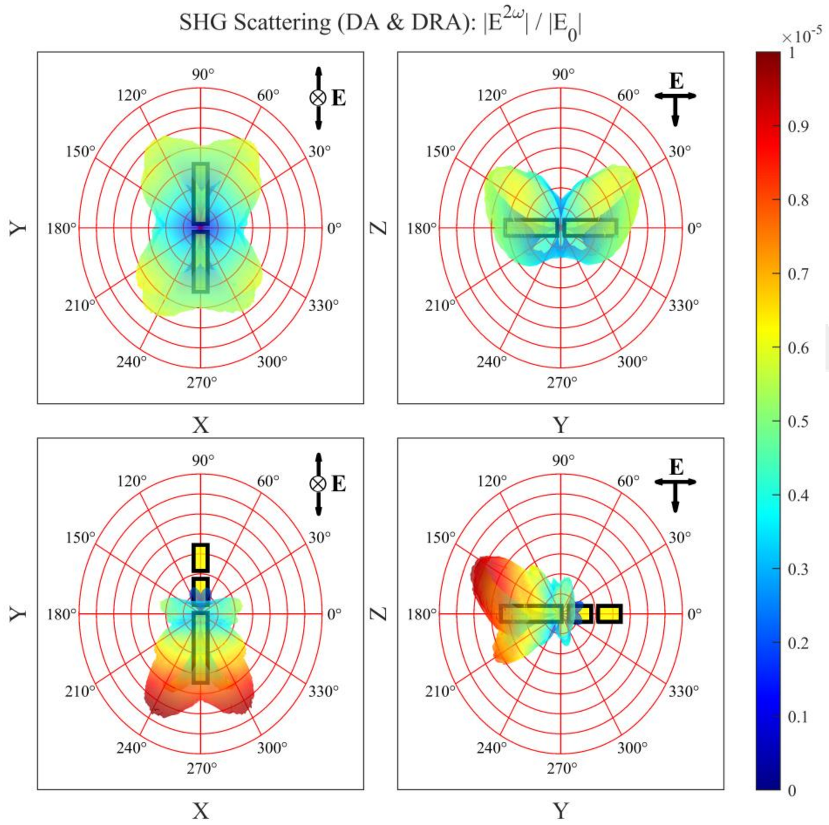

Figure 7.1: Far-field scattering plot of dipole and doubly resonant antennae.

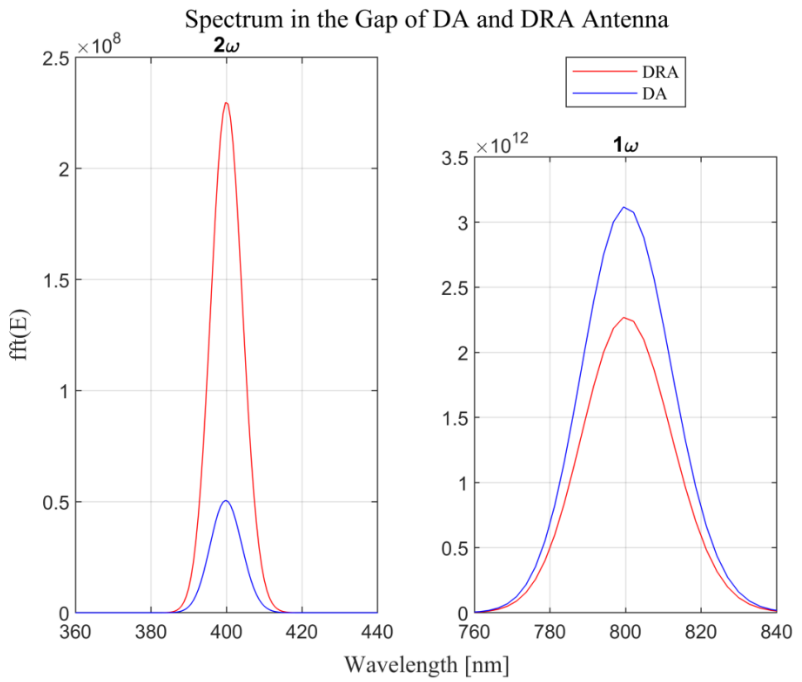

Figure 7.2: Near-field spectrum in the gap of the two antennae.

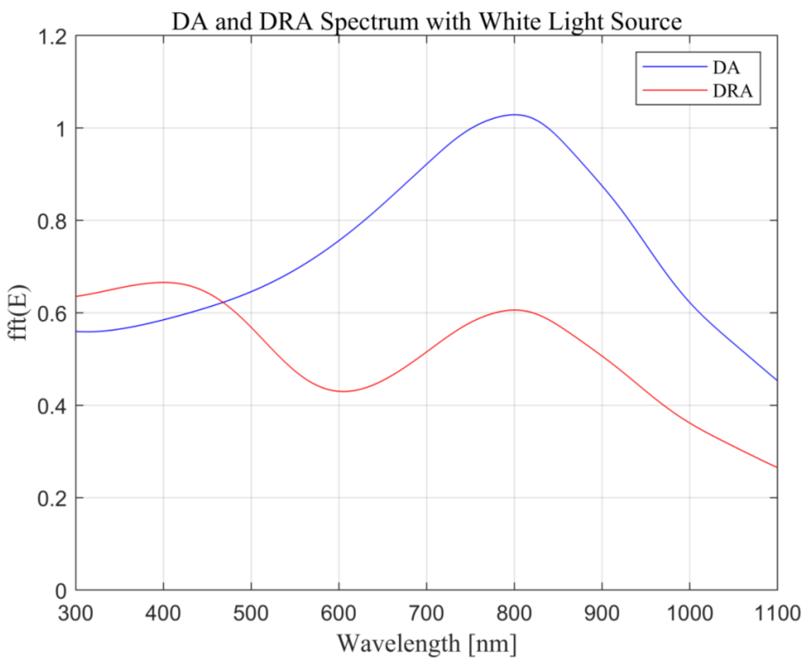

Figure 7.3: The linear (low intensity) spectrum of the two antennae.

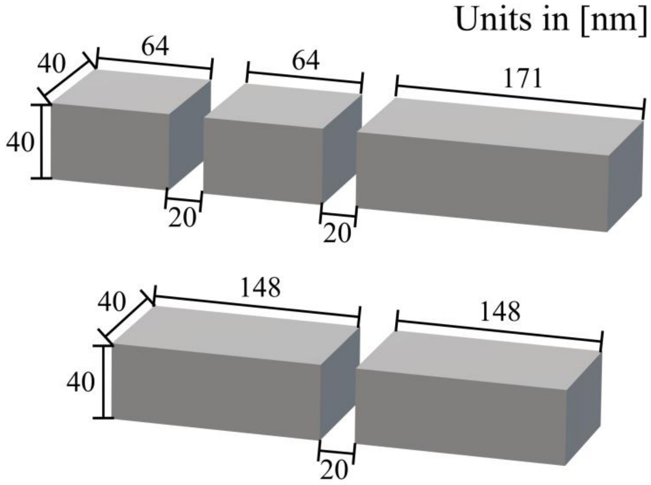

Figure 7.4: Geometry of dipole (bottom) and doubly resonant (top) antennae.

CHAPTER 8

INFINITELY LONG 2D GOLD NANORODS

Ginzburg et al. [17] simulated 2D nanorods using a similar set of hydrodynamic equations as in Equations 1.6.1-1.6.5. No use of boundary conditions was mentioned. Figure 8.1 illustrates the results of the same infinitely long gold nanorod with a radius r=100 nm. The excitation source is illuminating the nanorod along its short axis. Since the simulation is 2D and the rod is infinitely long, it has no resonance along its long axis. Figure 8.1 is not a cross-section as in previous 3D results. The results are very similar to the results of Ginzburg. Comparatively, Ginzburg's electric fields (especially THG) are smeared out, which probably indicates that an FDTD method was used (the method used was not stated). Sukharev's FDTD results [27] are likewise smeared. The electric fields in Figure 8.1 are of higher resolution and are confined to the surface, and the nanorod's interior is almost noise-free compared to Ginzburg.

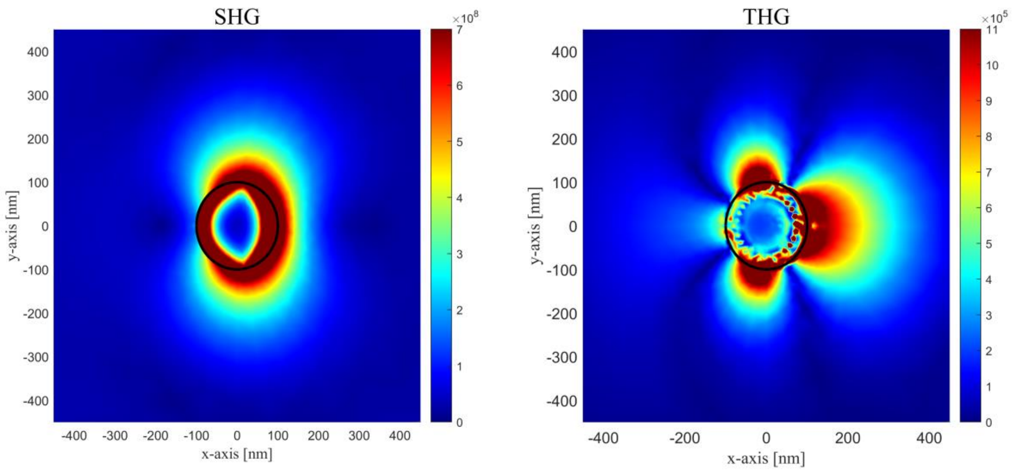

Figure 8.1: Simulation of infinitely long nanorods with a radius of 100 nm.

CHAPTER 9

CONCLUSION

The optical properties of gold ellipsoids with different aspect ratios are investigated under intense illumination using a set of hydrodynamical equations. The investigated optical properties of the gold nano ellipsoid are its spectra, near and far-fields, higher-order susceptibility maps, and four/five-wave mixing.

The simulated near-field results are spherical harmonics located mainly at the tips and corners of the gold nano ellipsoids and rods. The hydrodynamical equations and the spherical harmonics indicate that unique energy states exist on metal nanoparticles during intense illumination. The scattered far-field modes are extracted and consist of vector spherical harmonics, in line with Mie theory. The spectra of the nonlinear response show that the second and third harmonic generation are quadratically and cubically dependent on the incident power. Furthermore, the FWHM of the second and third harmonic generation are shorter than the fundamental pulse, following expected values.

Free electron-dependent higher-order susceptibility maps are important for second and higher-even-order nonlinearities. Post-processed susceptibility maps reveal that greater surface area and sharp features increase the higher-order susceptibility. Generally, susceptibility values are $\chi^{(2)} \approx 10^{-12}\ m/V$, and $\chi^{(3)} \approx 10^{-24}\ m^2/V^2$. Sharp and flanged tips have an order of magnitude higher and lower second-order susceptibilities, respectively.

The study is extended to three, four, and five-wave mixing. The four and five mixed wave conversion efficiencies compare favorably with existing semiconducting microring resonators. Maintaining quantum properties in a lossy medium such as gold is uncertain. However, studies have shown that single-particle and collective dynamics can coexist, and the coherence times of gold nanoparticles have been calculated to the order of hundreds of femtoseconds. It is not perfectly clear if quantum states can last long enough in gold to perform quantum operations practically. Still, the hydrodynamical model shows that an intensely illuminated Fermi gas in a gold nano ellipsoid can produce entangled states if the excited electrons in gold can hold quantum information within a reasonable period.

REFERENCES

[1] P. A. Franken and J. F. Ward, "Optical Harmonics and Nonlinear Phenomena," *Rev. Mod. Phys.*, vol. 35, no. 1, pp. 23-39. doi: 10.1103/RevModPhys.35.23, 1963.

[2] C. Fuentes-Hernandez, G. Ramos-Ortiz, S.-Y. Tseng, M. P. Gaj and B. Kippelen, "Third-harmonic generation and its applications in optical image processing," *J. Mater. Chem.*, vol. 19, no. 40, pp. 7394-7401. doi: 10.1039/B905561D, 2006.

[3] Z. Ge, Z.-Y. Zhou, J.-X. Cheng, L. Chen, Y.-H. Li, Y. Li, S.-J. Niu and B.-S. Shi, "Thermal camera based on frequency upconversion and its noise-equivalent temperature difference characterization," *Advanced Photonics Nexus*, vol. 2, no. 4, p. 046002. doi: 10.1117/1.APN.2.4.046002, 2023.

[4] M. Kauranen and A. V. Zayats, "Nonlinear plasmonics," *Nature Photonics*, vol. 6, no. 11, pp. 739-748. doi:10.1038/nphoton.2012.244, 2012.

[5] T. Liu, S. Xiao, B. Li, M. Gu, H. Luan and X. Fang, "Third- and Second-Harmonic Generation in All-Dielectric Nanostructures: A Mini Review," *Frontiers in Nanotechnology*, vol. 4, p. 891892. doi:10.3389/fnano.2022.891892, 2022.

[6] S. Sederberg, C. J. Firby and A. Y. Elezzabi, "Efficient, broadband third-harmonic generation in silicon nanophotonic waveguides spectrally shaped by nonlinear propagation," *Opt. Express*, vol. 27, no. 4, pp. 4990-5004. doi: 10.1364/OE.27.004990, Feb 2019.

[7] G. Grinblat, Y. Li, M. P. Nielsen, R. F. Oulton and S. A. Maier, "Efficient Third Harmonic Generation and Nonlinear Subwavelength Imaging at a Higher-Order Anapole Mode in a Single Germanium Nanodisk," *ACS Nano*, vol. 11, no. 1, pp. 953-960. doi: 10.1021/acsnano.6b07568, 24 Jan 2017.

[8] R. Xie, X. He, W. Wang, L. Zheng and J. Shi, "Efficient Third Harmonic Generation from Magnetic Resonance in Low-Index Dielectric Nanopillars," *Photonics,* vol. 11, no. 2, pp. 159-168. doi: 10.3390/photonics11020159, 2024.

[9] K. Thyagarajan, S. Rivier, A. Lovera and O. J. Martin, "Enhanced second-harmonic generation from double resonant plasmonic antennae," *Opt. Express,* vol. 20, no. 12, pp. 12860-12865. doi:10.1364/OE.20.012860, Jun 2012.

[10] U. Kreibig and M. Vollmer, Optical Properties of Metal Clusters, vol. 1, Heidelberg: Springer Berlin, 1995, pp. doi:10.1007/978-3-662-09109-8.

[11] K. Kolwas and A. Derkachova, "Damping rates of surface plasmons for particles of size from nano- to micrometers; reduction of the nonradiative decay," *Journal of Quantitative Spectroscopy and Radiative Transfer,* vol. 114, pp. 45-55. doi: 10.1016/j.jqsrt.2012.08.007, 2013.

[12] J. Sone, J. Fujita, Y. Ochiai, S. Manako, S. Matsui, E. Nomura, T. Baba, H. Kawaura, T. Sakamoto, C. D. Chen, Y. Nakamura and J. S. Tsai, "Nanofabrication toward sub-10 nm and its application to novel nanodevices," *Nanotechnology,* vol. 10, no. 2, pp. 135-141. doi:10.1088/0957-4484/10/2/306, Jun 1999.

[13] M. Decker, R. Zhao, C. M. Soukoulis, S. Linden and M. Wegener, "Twisted split-ring-resonator photonic metamaterial with huge optical activity," *Opt. Lett.,* vol. 35, no. 10, pp. 1593-1595. doi: 10.1364/OL.35.001593, May 2010.

[14] K. D. Ko, A. Kumar, K. H. Fung, R. Ambekar, G. L. Liu, N. X. Fang and K. C. J. Toussaint, "Nonlinear Optical Response from Arrays of Au Bowtie Nanoantennas," *Nano Letters,* vol. 11, no. 1, pp. 61-65. doi: 10.1021/nl102751m, 12 Jan 2011.

[15] E. Moreno, H. D. Nguyen, R. Stoian and J.-P. Colombier, "Full Explicit Numerical Modeling in Time-Domain for Nonlinear Electromagnetics

Simulations in Ultrafast Laser Nanostructuring," *Applied Sciences*, vol. 11, no. 16, pp. 7429-7453. doi: 10.3390/app11167429, 2021.

[16] R. W. Boyd, Z. Shi and I. De Leon, "The third-order nonlinear optical susceptibility of gold," *Optics Communications,* vol. 326, pp. 74-79. doi:10.1016/j.optcom.2014.03.005, 2014.

[17] P. Ginzburg, A. V. Krasavin, G. A. Wurtz and A. V. Zayats, "Nonperturbative Hydrodynamic Model for Multiple Harmonics Generation in Metallic Nanostructures," *ACS Photonics,* vol. 2, no. 1, pp. 8-13. doi:10.1021/ph500362y, 2015.

[18] M. Fox, Optical properties of solids, Oxford: Oxford University Press, 2010.

[19] S. A. Maier, Plasmonics: Fundamentals and Applications, New York, NY: Springer US, 2007.

[20] I. Suarez, A. Ferrando, J. Marques-Hueso, A. Diez, R. Abargues, P. J. Rodriguez-Canto and J. P. Martinez-Pastor, "Propagation length enhancement of surface plasmon polaritons in gold nano-/micro-waveguides by the interference with photonic modes in the surrounding active dielectrics," *Nanophotonics,* vol. 6, no. 5, pp. 1109-1120. doi:10.1515/nanoph-2016-0166, 2017.

[21] H. Schantz, "Theory and Practice of Near-Field Electromagnetic Ranging," in *Proceedings of the 2012 International Technical Meeting of The Institute of Navigation*, Newport Beach, CA, 2012.

[22] B. J. Messinger, K. U. von Raben, R. K. Chang and P. W. Barber, "Local fields at the surface of noble-metal microspheres," *Phys. Rev. B,* vol. 24, no. 2, pp. 649-657. doi: 10.1103/PhysRevB.24.649, 1981.

[23] D. Gall, "Electron mean free path in elemental metals," *Journal of Applied*

Physics, vol. 119, no. 8, p. 085101. doi:10.1063/1.4942216, Feb 2016.

[24] K. Kolwas, "Optimization of Coherent Dynamics of Localized Surface Plasmons in Gold and Silver Nanospheres; Large Size Effects," *Materials,* vol. 16, no. 5, pp. 1801-1816. doi:10.3390/ma16051801, 2023.

[25] W. J. Ding, J. Z. J. Lim, H. T. B. Do, X. Xiong, Z. Mahfoud, C. E. Png, M. Bosman, L. K. Ang and L. Wu, "Particle simulation of plasmons," *Nanophotonics,* vol. 9, no. 10, pp. 3303-3313. doi:10.1515/nanoph-2020-0067, 2020.

[26] M. C. Frazer, "Spherical harmonic analysis of the Navier-Stokes equation in magnetofluid dynamics," *Physics of the Earth and Planetary Interiors,* vol. 8, no. 1, pp. 75-82. doi:10.1016/0031-9201(74)90112-5, 1974.

[27] C. Li, X. Lu, A. Srivastava, S. Storm, R. Gelfand, M. Pelton, M. Sukharev and H. Harutyunyan, "Second Harmonic Generation from a Single Plasmonic Nanorod Strongly Coupled to a WSe2 Monolayer," *Nano Letters,* vol. 21, no. 4, pp. 1599-1605, 2021.

[28] F. Hache, D. Ricard and C. Flytzanis, "Optical nonlinearities of small metal particles: surface-mediated resonance and quantum size effects," *J. Opt. Soc. Am. B,* vol. 3, no. 12, pp. 1647-1655. doi:10.1364/JOSAB.3.001647, Dec 1986.

[29] F. Hache, D. Ricard and C. Flytzanis, "The optical kerr effect in small metal particles and metal colloids: The case of gold," *Applied Physics A,* vol. 47, pp. 347-357. doi:10.1007/BF00615498, 1988.

[30] M. S. Verma, M. Kumar and M. Chandra, "Controlling second harmonic generation of gold nanorods: Surface area matters more than aspect ratio," *Chemical Physics Letters,* vol. 741, no. 16, p. 137112. doi:10.1016/j.cplett.2020.137112, 2020.

[31] H. M. Ngo, P. P. Nguyen and I. Ledoux-Rak, "Optimization of second harmonic generation of gold nanospheres and nanorods in aqueous solution: the dominant role of surface area," *Phys. Chem. Chem. Phys.*, vol. 18, no. 4, pp. 3352-3356. doi:10.1039/C5CP06850A, 2016.

[32] H. Minh Ngo, E. Drobnyh, M. Sukharev, Q. Khuong Vo, J. Zyss and I. Ledoux-Rak, "High Yield Synthesis and Quadratic Nonlinearities of Gold Nanoprisms in Solution: The Role of Corner Sharpness," *Israel Journal of Chemistry*, vol. 63, no. 12, p. e202200009. doi:10.1002/ijch.202200009, 2023.

[33] P. Susnjar, A. Demidovich, G. Kurdi, P. Cinquegrana, I. Nikolov, P. Sigalotti and M. B. Danailov, "A novel common-path scheme for fourth harmonic generation by ultrashort laser pulses," *Optics Communications*, vol. 528, p. 129031. doi: 10.1016/j.optcom.2022.129031, 2023.

[34] J.-Q. Wang, Y.-H. Yang, M. Li, H. Zhou, X.-B. Xu, J.-Z. Zhang, C.-H. Dong, G.-C. Guo and C.-L. Zou, "Synthetic five-wave mixing in an integrated microcavity for visible-telecom entanglement generation," *Nature Communications*, vol. 13, no. 1, pp. 6223-6230. doi: 10.1038/s41467-022-33914-5, 2022.

[35] M. Previde Massara, F. A. Sabattoli, F. Pirzio, M. Galli and D. Bajoni, "Four-wave mixing in a silicon microring resonator using a self-pumping geometry," *Appl. Phys. Lett.*, vol. 113, no. 12, p. 121111. doi: 10.1063/1.5038931, 2018.

[36] E. Townsend, A. Debrecht and G. W. Bryant, "Approaching the quantum limit for nanoplasmonics," *Journal of Materials Research*, vol. 30, no. 16, pp. 2389-2399. doi: 10.1557/jmr.2015.232, 01 Aug 2015.

[37] M.-P. Lord, M. Olivier, M. Bernier and R. Vallee, "Visible femtosecond fiber laser," *Optics Letters*, vol. 48, no. 14, pp. 3709-3712, 2023.

[38] Y. Liu, K. Zhong, A. Wang, M. Zhou, S. Li, L. Gao and Z. Zhang, "Optical

Terahertz Sources Based on Difference Frequency Generation in Nonlinear Crystals," *Crystals,* vol. 12, no. 7, p. doi:10.3390/cryst12070936, 2022.

[39] P. C. Strassmann, A. Martin, N. Gisin and M. Afzelius, "Spectral noise in frequency conversion from the visible to the telecommunication C-band," *Optics Express,* vol. 27, no. 10, pp. 14298-14307. doi:10.1364/OE.27.014298, 2019.

[40] X. Lu, G. Moille, A. Rao and K. Srinivasan, "Proposal for noise-free visible-telecom quantum frequency conversion through third-order sum and difference frequency generation," *Optics Letters,* vol. 46, no. 2, pp. 222-225. doi:10.1364/OL.412602, 2021.

[41] C. Humbert, T. Noblet, L. Dalstein, B. Busson and G. Barbillon, "Sum-Frequency Generation Spectroscopy of Plasmonic Nanomaterials: A Review.," *Materials,* vol. 12, no. 5, p. 836. doi:10.3390/ma12050836, 2019.

[42] M. Todeschini, A. Bastos da Silva Fanta, F. Jensen, J. B. Wagner and A. Han, "Influence of Ti and Cr Adhesion Layers on Ultrathin Au Films," *ACS Appl. Mater. Interfaces,* vol. 9, no. 42, pp. 37374-37385. doi: 10.1021/acsami.7b10136, 2017.

APPENDICES

A. Number Density

The total number of free electrons in the simulated ellipsoid equals to approximately $2.5 \cdot 10^7$ electrons. Figure A.1 shows the electron number density and surface accumulation under intense illumination. At intense illumination approximately 100 electrons accumulate at the tips of the nano ellipsoid. Under normal illumination intensities, far lower number densities are reached, which is equivalent to less than a electron.

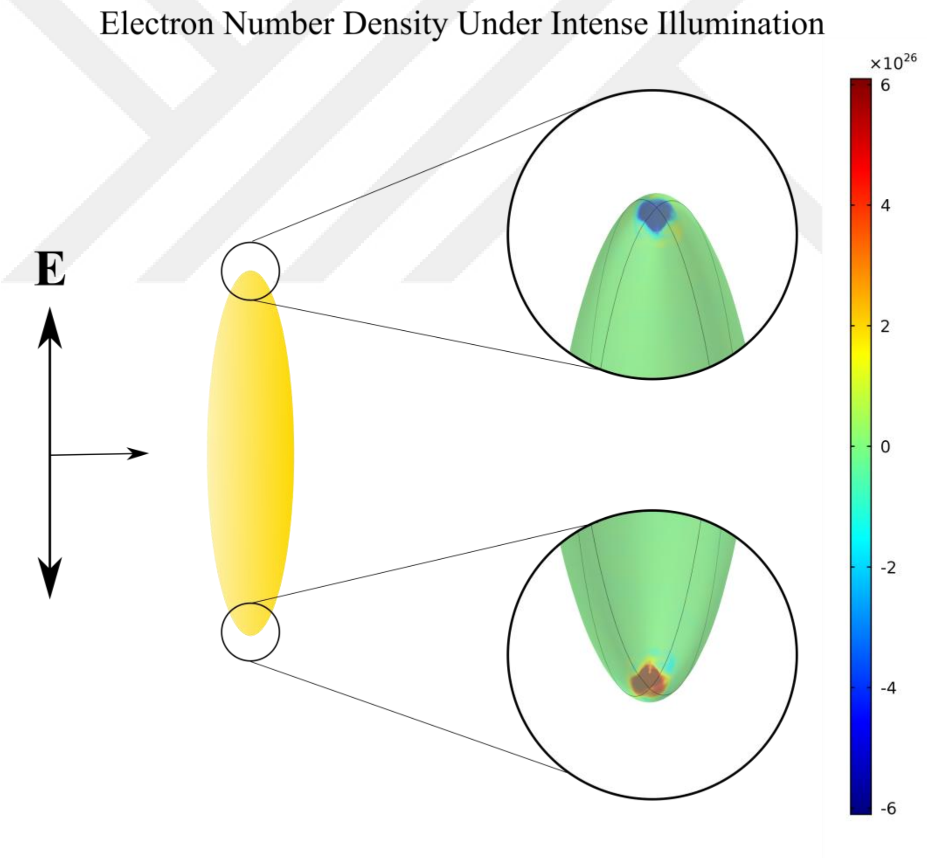

Figure A.1: Number density of electrons at the tips of the nano ellipsoid under intense illumination.

CURRICULUM VITAE

Surname, Name: Tepe, Hüseyin

EDUCATION

Degree	Institution	Year of Graduation
MS	Chalmers Applied Physics	2016
BS	Chalmers Engineering Physics	2016
High School	Kattegattgymnasiet, Halmstad	2011

INTERESTS

History, Philosophy, Photography, Saxophone, Clarinet, Basketball, Tennis

LANGUAGES

Swedish, English, Turkish